CrossMark

The Galaxy Activity, Torus, and Outflow Survey (GATOS). IV. Exploring Ionized Gas Outflows in Central Kiloparsec Regions of GATOS Seyferts

Lulu Zhang[1] , Chris Packham[1,2] , Erin K. S. Hicks[1,3,4] , Ric I. Davies[5] , Taro T. Shimizu[5] , Almudena Alonso-Herrero[6] ,
Laura Hermosa Muñoz[6], Ismael García-Bernete[6,7], Miguel Pereira-Santaella[8] , Anelise Audibert[9,10],
Enrique López-Rodríguez[11,12], Enrica Bellocchi[13,14], Andrew J. Bunker[7], Francoise Combes[15] , Tanio Díaz-Santos[16,17],
Poshak Gandhi[18] , Santiago García-Burillo[19], Begoña García-Lorenzo[9,10], Omaira González-Martín[20], Masatoshi Imanishi[21,22] ,
Alvaro Labiano[23], Mason T. Leist[1] , Nancy A. Levenson[24] , Cristina Ramos Almeida[9,10], Claudio Ricci[25,26] ,
Dimitra Rigopoulou[7,17] , David J. Rosario[27], Marko Stalevski[28,29] , Martin J. Ward[30], Donaji Esparza-Arredondo[9,10],
Dan Delaney[3,4], Lindsay Fuller[1], Houda Haidar[27], Sebastian Hönig[18], Takuma Izumi[21,22] , and Daniel Rouan[31]

[1] The University of Texas at San Antonio, One UTSA Circle, San Antonio, TX 78249, USA; lulu.zhang@utsa.edu, l.l.zhangastro@gmail.com
[2] National Astronomical Observatory of Japan, National Institutes of Natural Sciences (NINS), 2-21-1 Osawa, Mitaka, Tokyo 181-8588, Japan
[3] Department of Physics and Astronomy, University of Alaska Anchorage, Anchorage, AK 99508-4664, USA
[4] Department of Physics, University of Alaska, Fairbanks, AK 99775-5920, USA
[5] Max-Planck-Institut für extraterrestrische Physik, Postfach 1312, D-85741, Garching, Germany
[6] Centro de Astrobiología (CAB), CSIC-INTA, Camino Bajo del Castillo s/n, E-28692 Villanueva de la Cañada, Madrid, Spain
[7] Department of Physics, University of Oxford, Keble Road, Oxford OX1 3RH, UK
[8] Instituto de Física Fundamental, CSIC, Calle Serrano 123, 28006 Madrid, Spain
[9] Instituto de Astrofísica de Canarias, Calle Vía Láctea, s/n, E-38205, La Laguna, Tenerife, Spain
[10] Departamento de Astrofísica, Universidad de La Laguna, E-38206, La Laguna, Tenerife, Spain
[11] Kavli Institute for Particle Astrophysics & Cosmology (KIPAC), Stanford University, Stanford, CA 94305, USA
[12] Department of Physics & Astronomy, University of South Carolina, Columbia, SC 29208, USA
[13] Departmento de Física de la Tierra y Astroísica, Fac. de CC Físicas, Universidad Complutense de Madrid, E-28040 Madrid, Spain
[14] Instituto de Física de Partículas y del Cosmos IPARCOS, Fac. CC Físicas, Universidad Complutense de Madrid, E-28040 Madrid, Spain
[15] LERMA, Observatoire de Paris, Collège de France, PSL University, CNRS, Sorbonne University, Paris
[16] Institute of Astrophysics, Foundation for Research and Technology-Hellas (FORTH), Heraklion 70013, Greece
[17] School of Sciences, European University Cyprus, Diogenes street, Engomi, 1516 Nicosia, Cyprus
[18] School of Physics & Astronomy, University of Southampton, Hampshire SO17 1BJ, Southampton, UK
[19] Observatorio Astronómico Nacional (OAN-IGN)-Observatorio de Madrid, Alfonso XII, 3, 28014, Madrid, Spain
[20] Instituto de Radioastronomía and Astrofísica (IRyA-UNAM), 3-72 (Xangari), 8701, Morelia, Mexico
[21] National Astronomical Observatory of Japan, National Institutes of Natural Sciences, 2-21-1 Osawa, Mitaka, Tokyo 181-8588, Japan
[22] Department of Astronomy, School of Science, Graduate University for Advanced Studies (SOKENDAI), Mitaka, Tokyo 181-8588, Japan
[23] Telespazio UK for the European Space Agency (ESA), ESAC, Camino Bajo del Castillo s/n, 28692 Villanueva de la Cañada, Spain
[24] Space Telescope Science Institute, 3700 San Martin Drive Baltimore, MD 21218, USA
[25] Instituto de Estudios Astrofísicos, Facultad de Ingeniería y Ciencias, Universidad Diego Portales, Av. Ejército Libertador 441, Santiago, Chile
[26] Kavli Institute for Astronomy and Astrophysics, Peking University, Beijing 100871, People's Republic of China
[27] School of Mathematics, Statistics and Physics, Newcastle University, Newcastle upon Tyne, NE1 7RU, UK
[28] Astronomical Observatory, Volgina 7, 11060 Belgrade, Serbia
[29] Sterrenkundig Observatorium, Universiteit Gent, Krijgslaan 281-S9, Gent B-9000, Belgium
[30] Centre for Extragalactic Astronomy, Durham University, South Road, Durham DH1 3LE, UK
[31] LESIA, Observatoire de Paris, Université PSL, CNRS, Sorbonne Université, Sorbonne Paris Citeé, 5 place Jules Janssen, 92195 Meudon, France

Abstract

Utilizing JWST MIRI/Medium Resolution Spectrograph integral field unit observations of the kiloparsec-scale central regions, we showcase the diversity of ionized gas distributions and kinematics in six nearby Seyfert galaxies included in the GATOS survey. Specifically, we present spatially resolved flux distribution and velocity field maps of six ionized emission lines covering a large range of ionization potentials (15.8–97.1 eV). Based on these maps, we showcase the evidence of ionized gas outflows in the six targets, and find some highly disturbed regions in NGC 5728, NGC 5506, and ESO137-G034. We propose active galactic nucleus (AGN)-driven radio jets plausibly play an important role in triggering these highly disturbed regions. With the outflow rates estimated based on [Ne V] emission, we find the six targets tend to have ionized outflow rates converged to a narrower range than the previous finding. These results have an important implication for the outflow properties in AGN of comparable luminosity.

Materials only available in the online version of record: *machine-readable table*

1. Introduction

An important signature of feedback effects in galaxy evolution is gas outflows in different phases over diverse scales, which are frequently observed in nearby and distant galaxies of different types (e.g., Müller-Sánchez et al. 2011; Bellocchi et al. 2013; Veilleux et al. 2013; Arribas et al. 2014; Cicone et al. 2014;

García-Burillo et al. 2014, 2021; Harrison et al. 2014, 2018; Concas et al. 2019; Förster Schreiber et al. 2019; Freeman et al. 2019; Leung et al. 2019; Veilleux et al. 2020; Ramos Almeida et al. 2022; Maksym et al. 2023; Winkel et al. 2023). The role of such outflows in galaxy evolution is crucial as they regulate and/ or even quench both star formation and black hole activity by heating up cold gas and/or expelling it from the host galaxy (e.g., Schawinski et al. 2007; Page et al. 2012; Cheung et al. 2016; Harrison 2017; also see review by Veilleux et al. 2005; Fabian 2012; Somerville & Davé 2015; Harrison & Ramos Almeida 2024). Moreover, gas outflows are primarily responsible for the redistributing of dust and metals over large scales within a galaxy and even outside a galaxy in circumgalactic and intergalactic environments (e.g., Heckman et al. 1990; Melioli et al. 2015).

Active galactic nucleus (AGN) activity is required to drive the strongest outflows, some of which are powerful enough to rapidly suppress star formation in their host galaxies, particularly for the evolution of massive galaxies (e.g., Benson et al. 2003; McCarthy et al. 2011; Cano-Díaz et al. 2012; Davies et al. 2020a). Gas outflows are also of great importance in starburst systems, especially for star-forming galaxies during the peak epoch of star formation and black hole growth (redshift of $\sim$1–3, e.g., Shapley et al. 2003; Weiner et al. 2009; Rubin et al. 2014; Harrison et al. 2016; Förster Schreiber et al. 2019). AGN activity can affect their hosts and large-scale surroundings through outflows via different modes of feedback. Specifically, luminous, highly accreting AGN inject enough radiative energy through winds/outflows that are able to efficiently expel the surrounding gas by the "quasar-mode" feedback (e.g., Di Matteo et al. 2005; Hopkins et al. 2008). Meanwhile, low-luminosity AGN showing low-level nuclear activity exhibit increasingly prominent signatures of jet-like outflows that can heat surrounding gas through shocks, interacting with their environment mainly via the "kinetic-mode" feedback (e.g., Weinberger et al. 2017; Davé et al. 2019; and see review by McNamara & Nulsen 2007).

Although the general theoretical framework of state-of-the-art cosmological simulations has shown the importance of outflows in reproducing observed properties of different galaxy populations, the relative role of outflow mechanisms is not fully understood, albeit with some studies on the dependence of outflow properties on galaxy properties such as host galaxy mass (e.g., Chisholm et al. 2017), star formation rate (e.g., Roberts-Borsani et al. 2020), and AGN luminosity (e.g., Fiore et al. 2017). Even for AGN of the same luminosity, gas outflow rates can vary by up to 2 orders of magnitude, illustrating the diversity of gas outflow properties (e.g., Baron & Netzer 2019; Davies et al. 2020b; Lamperti et al. 2022; Bessiere et al. 2024; Speranza et al. 2024). Zubovas & Nardini (2020) proposed this diversity results from the different duty cycles of AGN variability and outflow process, as AGN luminosity varies on a much shorter timescale than that of outflows. Additionally, Fischer et al. (2017, 2018) proposed this diversity is due to the different launching directions of gas outflows, with the outflow being most intense when the AGN is sufficiently tilted for the outflow to fully interact with the galactic disk (see also Ramos Almeida et al. 2022; Audibert et al. 2023).

High resolution spatially resolved observations of ionic and molecular emission lines are crucial to distinguish the above scenarios (e.g., García-Burillo et al. 2014, 2019; Shimizu et al. 2019; García-Bernete et al. 2021; Peralta de Arriba et al. 2023;

Esposito et al. 2024). At nuclear scales, the outflow duty cycle is more rapid so that the effect proposed by Zubovas & Nardini (2020) will be mitigated, and thus, outflow properties at different AGN luminosity can be reconsidered. High resolution observations directly resolve gas outflow launching directions, affording the opportunity to determine the influence of the launching direction on outflow properties. The Medium Resolution Spectrograph (MRS; Wells et al. 2015; Labiano et al. 2021; Argyriou et al. 2023) on the Mid-Infrared Instrument (MIRI; Rieke et al. 2015; Wright et al. 2015, 2023) of James Webb Space Telescope (JWST; Gardner et al. 2023; Rigby et al. 2023) provides an unprecedented opportunity with its excellent spectral/angular resolution and sensitivity to advance our understanding of the diverse outflow properties in innermost regions of AGN (e.g., García-Bernete et al. 2022a, 2024b; U et al. 2022; Armus et al. 2023; Zhang & Ho 2023).

Leveraging JWST/MRS observations of the innermost kiloparsec-scale regions of six nearby Seyferts with comparable luminosity, we reveal the diversity of their spatially resolved ionized gas kinematics and the evidence of their ionized gas outflows. Our final goal is to shed light on the relative outflow strength in AGN with comparable luminosity. This paper is accompanied by papers on individual targets of the six (Hermosa Muñoz et al. 2024a; Davies et al. 2024; Esparza-Arredondo et al. 2024; and D. Delany et al. 2024, in preparation; H. Haidar et al. 2024, in preparation). See also the specific study in E. Lopez-Rodriguez et al. (2024, in preparation) of the emission line contribution to extended mid-IR (MIR) emission, as well as the study in García-Bernete et al. (2024c) and Zhang et al. (2024) of broad polycyclic aromatic hydrocarbon (PAH) features, of the six targets. In this paper, Section 2 describes the targets, observations, and data processing steps. Section 3 provides the maps and analysis on the spatially resolved ionized gas kinematics and showcases the evidence of ionized gas outflows in the six targets. Section 4 discusses the possible physical mechanism responsible for some highly disturbed regions in our targets, and Section 5 presents a rather quantitative comparison of the ionized gas outflow strength among the six targets. Section 6 contains a summary with main conclusions.

2. Data and Line Properties

2.1. Targets and Observations

This paper is part of a series studying six type 1.9/2 Seyfert galaxies ($L_{bol} \approx 10^{43.4}$–$10^{44.3}$ erg s^{-1}) with MRS integral field unit (IFU) spectral observations obtained by the JWST cycle 1 General Observer (GO) program No. 1670 (PI: Shimizu, T. Taro). The six targets are part of the Galactic Activity, Torus, and Outflow Survey (GATOS; Alonso-Herrero et al. 2021; García-Burillo et al. 2021; García-Bernete et al. 2024a),[32] and some of their basic properties are summarized in Table 1. The full sample of GATOS is selected from the 70 month Swift's Burst Alert Telescope (BAT) All-Sky Hard X-Ray Survey (Baumgartner et al. 2013), ensuring a nearly complete selection of AGN with the luminosities $L_{14-150\,keV} > 10^{42}$ erg s^{-1} at distances of 10–40 Mpc. The sample is largely unbiased to obscuration/absorption even up to column densities of $N_H \sim 10^{24}$ cm^{-2}. The AGN luminosity

---

[32] https://gatos.myportfolio.com

Table 1
Properties of the Sample

Galaxy	Type	z	D_L (Mpc)	i_{disk} (deg)	i_{cone} (deg)	$\log L_{bol}$ (erg s^{-1})	$\dot{M}_{out}$ ($M_\odot$ yr^{-1})	$\log \dot{E}_{kin}$ (erg s^{-1})	$\frac{L_{bol}}{L_{Edd}}$
(1)	(2)	(3)	(4)	(5)	(6)	(7)	(8)	(9)	(10)
NGC 5728	SAB(r)a	0.00932	39	43	49	44.1	0.09	40.3	0.05
NGC 5506	Sa pec	0.00608	27	80	42	44.1	0.21	40.6	0.04
ESO137-G034	SAB0/a	0.00914	35	38	⋯	43.4	0.52	40.7	0.01
NGC 7172	Sa pec	0.00868	37	88	67	44.1	0.005	38.4	0.02
MCG-05-23-016	S0	0.00849	35	66	50	44.3	0.003	37.8	0.06
NGC 3081	(R)SAB0/a(r)	0.00798	34	41	71	44.1	0.04	39.0	0.02

Note. Column (1): target name. Column (2): target host type from NASA/IPAC Extragalactic Database (NED), with (r) and (R) indicating inner and outer ring, respectively. Column (3): redshift taken from NED. Column (4): luminosity distance taken from NED using redshift independent estimates or peculiar velocity corrections (Theureau et al. 2007). Column (5): Galactic disk inclination. Column (6): AGN ionization cone inclination assuming the cone is aligned with the torus. Columns (7)–(10): bolometric AGN luminosity derived from X-ray luminosity; ionized gas mass outflow rate and ionized outflow kinetic energy derived from [O III] 5007 Å emission, and Eddington ratio, respectively. References for column (5): NGC 5728 (Shimizu et al. 2019), NGC 5506 (Esposito et al. 2024), NGC 7172 (Alonso-Herrero et al. 2023), ESO137-G034, MCG-05-23-016, and NGC 3081 (Burtscher et al. 2021, galaxy axis ratios therein). References for column (6): NGC 5728 (Shimizu et al. 2019), NGC 5506 (Sun et al. 2018), NGC 7172 (Alonso-Herrero et al. 2023), MCG-05-23-016 (Zoghbi et al. 2017), and NGC 3081 (Ramos Almeida et al. 2011). Reference for columns (7)–(10): Davies et al. (2015, 2020b); Caglar et al. (2020).

and absorbing column density can be obtained by the analysis of the X-ray data (Ricci et al. 2017).

The MIRI/MRS observations were carried out using the full set of four IFUs (channels 1–4), covering 4.9–7.6 μm, 7.51–11.71 μm, 11.55–17.98 μm, and 17.7–27.9 μm, respectively. These four channels are observed simultaneously, but each exposure can only cover one of the three grating settings (short, medium, and long subbands). The observational configuration and total science exposure time of each sampled Seyfert galaxy are summarized in Table 2. For background observations, a two-point dither pattern is taken for all targets, in a blank region of sky a few arcminutes away from the targets.

We primarily follow the standard JWST MIRI/MRS pipeline (release 1.11.4) to reduce the raw data (e.g., Labiano et al. 2016; Bushouse et al. 2023), using the same configuration (the calibration context 1130) of the pipeline stages as is in García-Bernete et al. (2022a) and Pereira-Santaella et al. (2022). Residual fringes remain with the standard fringe removal, which could have a significant influence on weak spectral features (Argyriou et al. 2020; Gasman et al. 2023). Therefore, we apply an extra JWST pipeline step (i.e., residual_fringe) not implemented in the standard JWST pipeline to correct the low-frequency fringe residuals (Law et al. 2023), before performing the standard process to generate the 3D spectral data cubes. Moreover, some hot and cold pixels are not identified by the current pipeline version, so we also added an extra step before creating the data cubes to mask them. The data reduction and extra steps are described in García-Bernete et al. (2024a).

2.2. Data Analysis

Zhang et al. (2021) developed a strategy for spatially resolved analysis of mid-infrared (mid-IR) properties of nearby galaxies, based on the mapping-mode observations taken with the Infrared Spectrograph (IRS; Houck et al. 2004) on Spitzer Space Telescope (Werner et al. 2004). This strategy, as summarized below, has already been applied to investigate the interaction between AGN and starburst activity in the central ~1.5 kpc × 1.3 kpc region of type 1 Seyfert galaxy NGC 7469 on a ~100 pc scale, based on JWST MIRI/MRS IFU observations (Zhang & Ho 2023). We

Table 2
Observational Configurations of the Sample

Target	R.A. (deg)	Decl. (deg)	Mosaic	Dither	t_{Exp} (s)
(1)	(2)	(3)	(4)	(5)	(6)
NGC 5728	14:42:23.880	−17:15:11.08	2 × 2	Four point	1051
NGC 5506	14:13:14.878	−03:12:27.76	1 × 8	None	275
ESO137-G034	16:35:13.995	−58:04:47.91	2 × 1	Four point	1147
NGC 7172	22:02:1.889	−31:52:10.47	None	Four point	1121
MCG-05-23-016	09:47:40.135	−30:56:56.00	None	Four point	1121
NGC 3081	09:59:29.534	−22:49:34.78	2 × 2	Four point	1147

Note. Column (1): target name. Column (2): R.A. of target. Column (3): decl. of target. Column (4): mosaic pattern. Column (5): dither strategy. Column (6): total exposure time of each subband.

adopt the same strategy to study ionized gas kinematics in central kiloparsec-scale regions of the six Seyfert galaxies (see Figure 1).

A key step of this strategy for extracting spatially resolved diagnostics on a common physical scale is to have the same angular resolution for all the slices within MIRI/MRS data cubes. To this end, we need to convolve all the slices within different data cubes of each sampled Seyfert galaxy to have the same angular resolution as the slice of the widest point-spread function (PSF). We focus on the first three channels (i.e., channels 1, 2, and 3; $\lambda \approx 5$–18 μm) to have as high of a full width at half maximum (FWHM) angular resolution as possible (i.e., FWHM ≈ 0″.3 − 0″.7), while covering all the emission lines relevant for this study. Based on the measured PSF FWHMs of JWST/MRS observations as detailed in Zhang & Ho (2023), we use a two-dimensional Gaussian function to mimic the PSF of each slice and then construct the convolution kernels (Aniano et al. 2011). After convolving all slices to the same angular resolution, of 0″.7, we reproject all spectral data cubes into the same coordinate frame with a pixel size of 0″.35 (half of the angular resolution, ~45–70 pc at distances of the targets), for further spectrum extraction and emission line fitting.
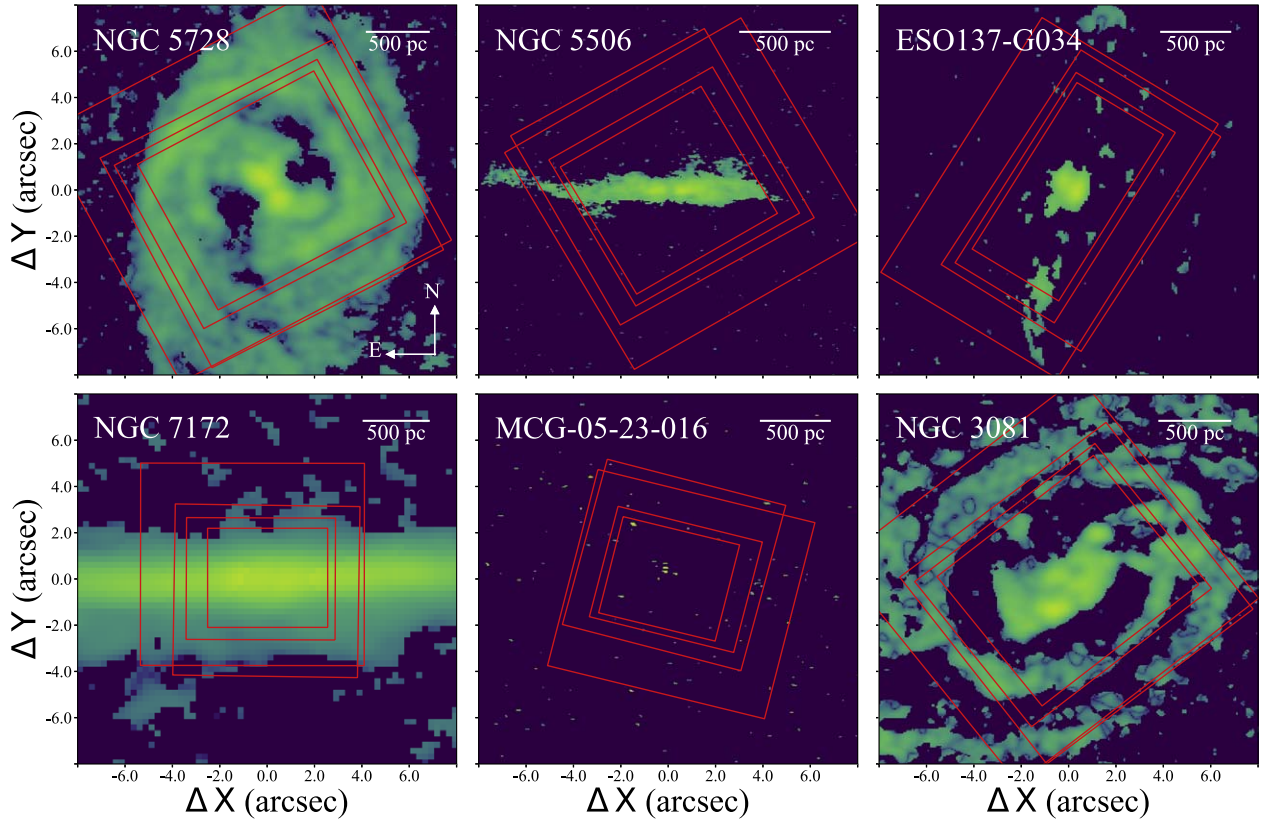
Figure 1. Illustration of channel 1–4 (red rectangles from small to large) MIRI/MRS coverages of the six Seyfert galaxies, with Atacama Large Millimeter/submillimeter Array CO(2-1) maps (see acknowledgments) as the background. A scale bar of 500 pc is in the top right of each panel, and a compass is in the top left panel and is the same for all panels, with N is up, and E is to the left.

2.3. Emission Line Fitting

Mid-IR spectra of galaxies exhibit abundant ionic fine-structure lines and molecular hydrogen rotational lines that are well resolved with the spectral resolution of JWST/MRS. In general, the relative strength and broadening of emission lines provide valuable diagnostics of galaxy properties (e.g., Pereira-Santaella et al. 2010, 2017; D'Agostino et al. 2019; Sajina et al. 2022; Feltre et al. 2023). This paper focuses on six ionized emission lines covering a large range of ionization potentials (i.e., [Ar II] 6.985 μm, [Ne II] 12.814 μm, [Ar III] 8.991 μm, [S IV] 10.511 μm, [Ne III] 15.555 μm, and [Ne V] 14.322 μm lines with ionization potentials ranging from 15.8 to 97.1 eV, see Table 3). In this work, we fit each ionic emission line using a single- and then a double-Gaussian profile, plus a local linear continuum. The fitting is implemented with the Levenberg–Marquardt least-squares minimization algorithm. Based on the reduced χ^2 values of the two sets of fitting, we calculate the p-value using a statistical F-test and only adopt the double-Gaussian fitting result if $p < 0.05$ (see also Hao et al. 2005). Stronger constraints tend to include only one Gaussian component in the best-fit profile for some low signal-to-noise spaxels, but will not affect our conclusions. To get more robust statistics, each emission line is perturbed with random noise at its uncertainty level, and then, the fitting is repeated 100 times. The median and standard deviation of those 100 fits are taken as the final estimate and corresponding uncertainty of each emission line, respectively.

2.4. Nonparametric Measurement

As shown in Figure 2, emission lines of certain spaxels of our targets exhibit a double-peaked profile. Such double-peaked profiles are caused by outflows with disturbed velocity field as will be detailed later (e.g., Fischer et al. 2011; Bae & Woo 2016). In such cases, certain bias will occur when assigning the broader component of the best-fit result to outflow-dominated motions. Therefore, to provide consistent measurements for all the six targets, in this work, we adopt the nonparametric methodology to study the kinematics of the six targets (Rupke & Veilleux 2011; Liu et al. 2013; Harrison et al. 2014; McElroy et al. 2015; Hervella Seoane et al. 2023). Similar to previous studies leveraging nonparametric measurements (e.g., Liu et al. 2013; Harrison et al. 2014; McElroy et al. 2015; Speranza et al. 2024), we derive the nonparametric velocities (Figure 2) based on the best-fit profile of each emission line to address low signal-to-noise regions. This work focuses on $v_{\rm m}$, the velocity that bisects the area under the emission line profile, and W_{80}, the line width that contains the central 80% of the flux as $W_{80} = v_{90} - v_{10}$, where v_{10} and v_{90} are velocities corresponding to 10% and 90% of the line flux, respectively.

The nonparametric methodology diagnoses the flux-weighted motion, i.e., the primary motion, of the gas component. Thus, this methodology is good at distinguishing line emission that is sensitive to gas outflows from that sensitive to gas rotation. Meanwhile, for more general cases (as is in companion papers on individual targets), the parametric methodology is also widely

Table 3
Measurements for Emission Lines Furnished on Spectra Extracted from Central Apertures

Line	λ (μm)	IP (eV)	NGC 5728		NGC 5506		ESO137-G034		NGC 7172		MCG-05-23-016		NGC 3081	
			Log Flux (ergs s^{-1} cm^{-2})	W_{80} (km s^{-1})	Log Flux (ergs s^{-1} cm^{-2})	W_{80} (km s^{-1})	Log Flux (ergs s^{-1} cm^{-2})	W_{80} (km s^{-1})	Log Flux (ergs s^{-1} cm^{-2})	W_{80} (km s^{-1})	Log Flux (ergs s^{-1} cm^{-2})	W_{80} (km s^{-1})	Log Flux (ergs s^{-1} cm^{-2})	W_{80} (km s^{-1})
(1)	(2)	(3)	(4)	(5)	(6)	(7)	(8)	(9)	(10)	(11)	(12)	(13)	(14)	(15)
H_2 S(8)	5.053	···	−14.54(0.02)	366.2 (13.0)	−14.61(0.35)	219.2 (2763.0)	−14.69(0.18)	434.1 (2127.0)	−14.91(0.36)	236.2 (1146.0)	−15.02(0.05)	229.1 (1022.0)	−14.87(0.03)	247.3 (12.3)
[Fe II]	5.34	7.9	−14.05(0.01)	535.4 (11.3)	−13.23(0.01)	411.6 (11.8)	−13.89(0.01)	634.9 (14.0)	−14.18(0.03)	312.8 (20.4)	−14.51(0.03)	303.6 (16.1)	−14.66(0.02)	236.9 (14.3)
[Fe VIII]	5.447	124	−14.03(0.02)	664.9 (11.9)	−13.60(0.06)	1196.0 (56.8)	−14.17(0.06)	510.8(6.5)	−15.17(1.09)	241.5 (205.0)	−13.64(0.08)	275.7(5.2)	−13.60(0.01)	561.3(6.5)
[Mg VII]	5.503	186.5	−13.97(0.27)	584.4 (326.0)	−13.61(0.14)	1186.0 (272.5)	−13.88(0.22)	732.6 (4242.0)	−14.25(0.23)	331.2 (935.8)	−13.54(0.18)	342.6 (1404.0)	−13.58(0.11)	778.6 (612.6)
H_2 S(7)	5.511	···	−13.78(0.16)	399.0 (1387.0)	−13.67(0.11)	260.6 (1246.0)	−14.36(0.20)	207.3 (1412.0)	−14.22(0.14)	464.6 (139.1)	−14.33(0.57)	689.7 (3282.0)	−14.49(1.20)	249.5 (484.6)
[Mg V]	5.61	109.2	−13.57(0.04)	750.1(6.4)	−12.95(0.03)	1470.0 (229.5)	−13.80(0.06)	535.1(5.6)	−13.81(0.02)	336.0 (12.1)	−13.61(0.09)	283.3 (12.4)	−13.43(0.03)	492.2 (17.4)
H_2 S(6)	6.109	···	−14.39(0.12)	370.0(9.2)	−14.29(0.01)	207.9(5.4)	−14.43(0.19)	302.0(4.4)	−14.83(0.09)	315.4 (83.0)	−14.82(0.03)	207.1 (11.9)	−14.78(0.02)	228.4(8.6)
H_2 S(5)	6.91	···	−13.63(0.09)	398.3(5.1)	−13.46(0.00)	238.4(2.8)	−13.74(0.01)	332.8(4.6)	−14.16(0.01)	327.0(7.7)	−14.12(0.02)	221.1(9.0)	−14.03(0.02)	257.2(7.7)
[Ar II]	6.985	15.8	−13.49(0.02)	451.1(5.9)	−12.77(0.01)	471.3(3.4)	−13.51(0.05)	485.7(3.8)	−13.59(0.15)	283.3 (91.2)	−13.27(0.12)	238.6(3.0)	−13.65(0.11)	263.5(3.2)
[Na III]	7.318	47.3	−14.27(0.01)	614.3 (17.4)	−13.96(0.02)	456.3 (45.8)	−14.56(0.01)	592.1 (14.5)	−14.34(0.02)	417.9 (27.3)	−14.31(0.01)	257.5(9.4)	−14.39(0.01)	314.0 (11.7)
Pfα	7.46	13.6	−14.60(0.02)	562.5 (27.9)	−13.60(0.02)	678.0 (30.5)	−14.50(0.02)	684.9 (21.8)	−14.54(0.20)	341.3 (237.3)	−14.03(0.07)	591.4 (94.8)	−14.75(0.05)	246.4 (26.8)
[Ne VI]	7.652	126.2	−12.96(0.06)	623.6(9.8)	−12.52(0.02)	945.4 (32.0)	−13.13(0.17)	492.1 (13.0)	−13.16(0.01)	300.0(4.9)	−12.67(0.01)	241.9(4.3)	−12.87(0.01)	445.7(5.7)
[Fe VII]	7.815	99.1	−14.31(0.01)	822.3 (16.2)	−13.48(0.03)	1849.0 (115.8)	−14.37(0.08)	567.3 (15.7)	···	···	−14.09(0.02)	271.4 (16.7)	−13.91(0.13)	563.7 (15.6)
[Ar V]	7.902	40.7	−14.18(0.14)	697.8 (404.3)	−13.56(0.03)	883.3 (55.6)	−14.28(0.10)	518.4 (93.5)	−14.54(0.03)	268.7 (14.3)	−14.08(0.04)	442.4 (140.1)	−14.20(0.03)	392.2 (44.0)
H_2 S(4)	8.025	···	−13.97(0.09)	414.0(7.3)	−13.85(0.01)	261.3 (12.7)	−14.08(0.01)	331.8(3.5)	−14.42(0.03)	409.6 (33.2)	−14.44(0.02)	254.0 (15.0)	−14.39(0.02)	250.4(9.7)
[Ar III]	8.991	27.6	−13.66(0.02)	636.4(7.0)	−12.96(0.01)	697.5(8.3)	−13.58(0.04)	528.9(2.6)	−14.00(0.18)	310.4 (10.6)	−13.43(0.06)	270.0(7.0)	−13.45(0.01)	427.0(9.9)
[Fe VII]	9.527	99.1	−14.31(0.12)	784.8 (43.0)	−13.70(0.02)	961.5 (13.3)	−14.24(0.08)	593.1(6.6)	−14.94(0.03)	355.6 (24.7)	−14.03(0.03)	305.8 (33.6)	−13.73(0.02)	557.6(4.7)
H_2 S(3)	9.665	···	−13.86(0.07)	433.6(7.4)	−13.70(0.01)	245.2(6.7)	−13.76(0.01)	330.6(3.5)	−14.60(0.02)	314.3 (19.5)	−14.02(0.01)	249.3(7.0)	−13.97(0.01)	241.9(6.6)
[S IV]	10.511	34.8	−13.03(0.01)	641.6(4.8)	−12.38(0.01)	655.9(7.4)	−12.90(0.03)	524.6(2.0)	−13.54(0.07)	347.5(9.4)	−13.28(0.03)	296.7 (217.5)	−12.89(0.00)	248.7(1.1)
H_2 S(2)	12.279	···	−14.06(0.15)	416.3 (26.6)	−13.92(0.02)	245.3 (13.0)	−14.22(0.01)	242.2(6.5)	−14.45(0.03)	269.4 (16.3)	−14.43(0.04)	221.7 (17.7)	−14.43(0.02)	234.5 (14.1)
Huα	12.37	13.6	−15.22 (0.03)	518.8 (37.3)	−14.28 (0.04)	502.9 (55.0)	−14.96 (0.02)	685.1 (35.4)	−14.91 (0.06)	641.6 (89.5)	−14.63 (0.09)	414.3 (120.6)	−15.15 (0.43)	313.3 (387.9)
[Ne II]	12.814	21.6	−13.13(0.15)	465.1 (13.1)	−12.45(0.01)	523.9 (11.1)	−13.20(0.20)	481.8(8.0)	−13.25(0.22)	333.9 (29.4)	−12.85(0.19)	241.2(3.6)	−13.30(0.03)	267.2(1.7)
[Ar V]	13.102	40.7	−14.22(0.02)	758.4 (17.8)	−13.42(0.09)	1414.0 (299.2)	−14.21(0.07)	522.5 (11.4)	−14.58(0.17)	254.9 (251.9)	−14.42(0.10)	181.9 (20.0)	−14.24(0.01)	208.5(3.0)

Table 3
(Continued)

Line	λ	IP	NGC 5728 Log Flux	W_{80}	NGC 5506 Log Flux	W_{80}	ESO137-G034 Log Flux	W_{80}	NGC 7172 Log Flux	W_{80}	MCG-05-23-016 Log Flux	W_{80}	NGC 3081 Log Flux	W_{80}
	(μm)	(eV)	(ergs s^{-1} cm^{-2})	(km s^{-1})	(ergs s^{-1} cm^{-2})	(km s^{-1})	(ergs s^{-1} cm^{-2})	(km s^{-1})	(ergs s^{-1} cm^{-2})	(km s^{-1})	(ergs s^{-1} cm^{-2})	(km s^{-1})	(ergs s^{-1} cm^{-2})	(km s^{-1})
(1)	(2)	(3)	(4)	(5)	(6)	(7)	(8)	(9)	(10)	(11)	(12)	(13)	(14)	(15)
[Ne V]	14.322	97.1	−13.04(0.02)	695.3(9.0)	−12.43(0.01)	896.6 (21.3)	−13.06(0.04)	517.7(3.4)	−13.22(0.19)	308.4(9.2)	−13.01(0.12)	248.8(4.5)	−12.94(0.01)	292.1(3.5)
[Ne III]	15.555	41.0	−12.79(0.06)	596.7(5.2)	−12.10(0.01)	655.5(6.5)	−12.76(0.02)	512.7(1.6)	−13.08(0.17)	316.2(4.9)	−12.87(0.15)	251.5(3.7)	−12.80(0.00)	275.5(0.7)
H$_2$ S(1)	17.035	⋯	−13.92(0.13)	399.6 (13.7)	−13.78(0.03)	231.5 (16.4)	−14.16(0.01)	236.4(4.1)	−14.25(0.01)	231.7 (10.8)	−14.16(0.04)	241.8 (25.6)	−14.19(0.02)	251.6 (10.0)
[S III]	18.71	23.3	−13.25(0.01)	634.6(9.7)	−12.55(0.01)	574.2 (10.1)	−13.12(0.04)	551.1(3.3)	−13.66(0.15)	302.9 (71.8)	−13.51(0.05)	241.8 (21.9)	−13.24(0.01)	258.4 (13.9)
[Ne V]	24.32	97.1	−13.16(0.02)	773.0 (13.1)	−12.67(0.05)	618.3 (30.8)	−13.11(0.07)	570.1(4.7)	−13.33(0.02)	364.1(9.2)	−13.18(0.05)	439.2 (120.6)	−13.03(0.01)	289.6(3.8)
[O IV]	25.89	54.9	−12.68(0.01)	751.6 (10.3)	−12.10(0.01)	648.3 (10.7)	−12.59(0.05)	562.9(2.4)	−12.87(0.02)	332.8(3.4)	−12.88(0.11)	326.0 (24.7)	−12.61(0.01)	275.8(1.8)

Note. Column (1): line name. Column (2): rest wavelength. Column (3): ionization potential (IP). Columns (4)–(15): the flux and W_{80} measurements (with the uncertainty in parentheses) of each emission line on the nuclear spectrum extracted from a $r = 0\rlap{.}{''}75$ aperture for each sampled Seyfert galaxy.

(This table is available in its entirety in machine-readable form in the online article.)
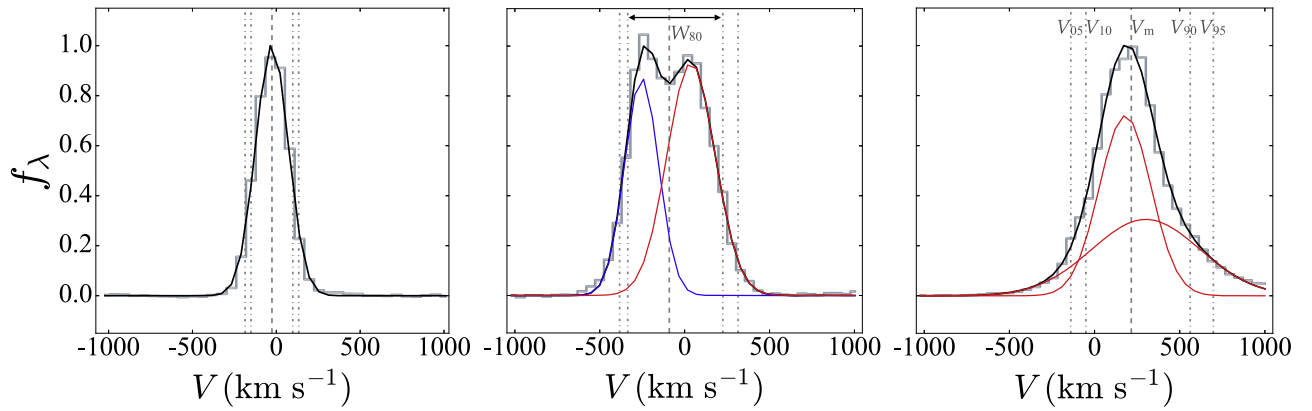
Figure 2. Illustration of emission line fitting for different observed line profiles, where gray histograms and black curves represent (with the local linear continuum subtracted) the observed and best-fitted emission line profiles, respectively. The blue and red curves further indicate separate Gaussian profiles if the emission line is better fitted with a double-Gaussian profile (blueshifted and/or redshifted). The vertical lines in each panel are, from left to right, v_{05}, v_{10}, v_{m}, v_{90}, and v_{95}, respectively, and the W_{80} is also indicated in the middle panel.

used. The parametric methodology considers individual Gaussian components in the best-fit profile separately, and provides a further separation of outflow-dominated components from rotation-dominated ones for emission lines that are dominated by gas rotation (e.g., Bellocchi et al. 2019; Leung et al. 2019; Cazzoli et al. 2020, 2022; Peralta de Arriba et al. 2023; Venturi et al. 2023; Hermosa Muñoz et al. 2024b). Therefore, a brief discussion on the ionized gas kinematics in central regions of the six targets based on the parametric methodology is also provided in Appendix A.

3. Characteristics of Ionized Gas Kinematics and Evidence of Ionized Gas Outflows

3.1. Extracted Spectra and Emission Line Measurements

To illustrate the rich information captured by JWST MIRI/MRS spectra, Figure 3 presents spectra extracted from $r = 0\rlap{.}{''}75$ apertures centered on the IR continuum peak (as the location of AGN) for each target. Channels 1, 2, and 3 spectra are extracted from the convolved spectral data cubes (Section 2.2), and channel 4 spectra are extracted from spectral data cubes without convolution. The extraction aperture radius (i.e., $0\rlap{.}{''}75$, ~100–150 pc at distances of the targets) for the four channels is large enough, and hence, no aperture correction was applied (as confirmed by the smooth transition from channel 3 to channel 4 spectra). These spectra exhibit diverse properties in terms of continuum shape and emission line intensity.

For example, the nuclear spectrum of NGC 7172 is different from others, which is attributable to the strong silicate absorption around 9.7 and 18 μm of a dust lane and/or hot dust around its nucleus (Smajić et al. 2012; Alonso-Herrero et al. 2021). More importantly, spectra in Figure 3 exhibit more narrow emission lines and the lacking of PAH features (see also García-Bernete et al. 2024a, 2024c), compared to Spitzer/IRS spectra (Asmus et al. 2014; García-Bernete et al. 2016). Table 3 provides the measured flux and W_{80} for 21 prominent ionized and 8 molecular lines from these spectra based on the nonparametric methodology (Sections 2.3 and 2.4). Specific measurements of relatively broad PAH features, which are diluted by the underlying continuum and could be destroyed by AGN (e.g., García-Bernete et al. 2022a, 2022b; Zhang et al. 2022; Ramos Almeida et al. 2023), will be presented

and studied in García-Bernete et al. (2024c) and Zhang et al. (2024).

In this paper, we focus on spatially resolved ionized gas kinematics targeting [Ar II], [Ne II], [Ar III], [S IV], [Ne III], and [Ne V] emission lines. Before the detailed analysis of the spatially resolved maps of these emission lines, we first look at the normalized profiles (with local continuum subtracted) of these six ionic emission lines from the above spectra. As shown in Figure 4, we find that NGC 5728, NGC 5506, and ESO137-G034 appear to display stronger signatures of disturbed ionized gas with broader emission line profiles ($W_{80} \gtrsim 500\,\mathrm{km\,s^{-1}}$) than NGC 7172, MCG-05-23-016, and NGC 3081 ($W_{80} \lesssim 400\,\mathrm{km\,s^{-1}}$). The widths of the observed line profiles include the contribution from instrumental broadening, which impacts the [Ne III] 15.555 μm line the most as it has the longest wavelength among the six emission lines (Labiano et al. 2021). Taking such effect into consideration for [Ne III] line will reduce W_{80} by less than 15% (10%) for measured W_{80} with values larger than $250\,\mathrm{km\,s^{-1}}$ ($300\,\mathrm{km\,s^{-1}}$), assuming a Gaussian profile.

High ionization lines exhibit stronger signatures of disturbed kinematics with relatively broader profiles and/or larger velocity shifts, compared to low ionization lines (see also Armus et al. 2023; Hermosa Muñoz et al. 2024a). Additionally, for the six targets, all H_2 rotational lines have $W_{80} \lesssim 300\,\mathrm{km\,s^{-1}}$, except for NGC 5728 with W_{80} of H_2 lines ~$400\,\mathrm{km\,s^{-1}}$ (Table 3). The relatively narrower H_2 lines against ionized emission lines are consistent with the result that the broadening of H_2 lines is more dominated by gravitational potential of a galaxy. Specific analysis of the H_2 lines of these targets is beyond the scope of this paper and is left to dedicated works in this series (i.e., Davies et al. 2024; Esparza-Arredondo et al. 2024; and particularly D. Delany et al. 2024, in preparation)

3.2. Spatially Resolved Ionized Gas Distributions and Kinematics

Based on nonparametric measurements for individual $0\rlap{.}{''}35 \times 0\rlap{.}{''}35$ spaxels in central regions of our targets, this section presents flux distributions and kinematics of the six emission lines covering a large range of ionization potentials. Based on the rather qualitative analysis as detailed below, we (1) showcase the evidence of ionized gas outflows along their
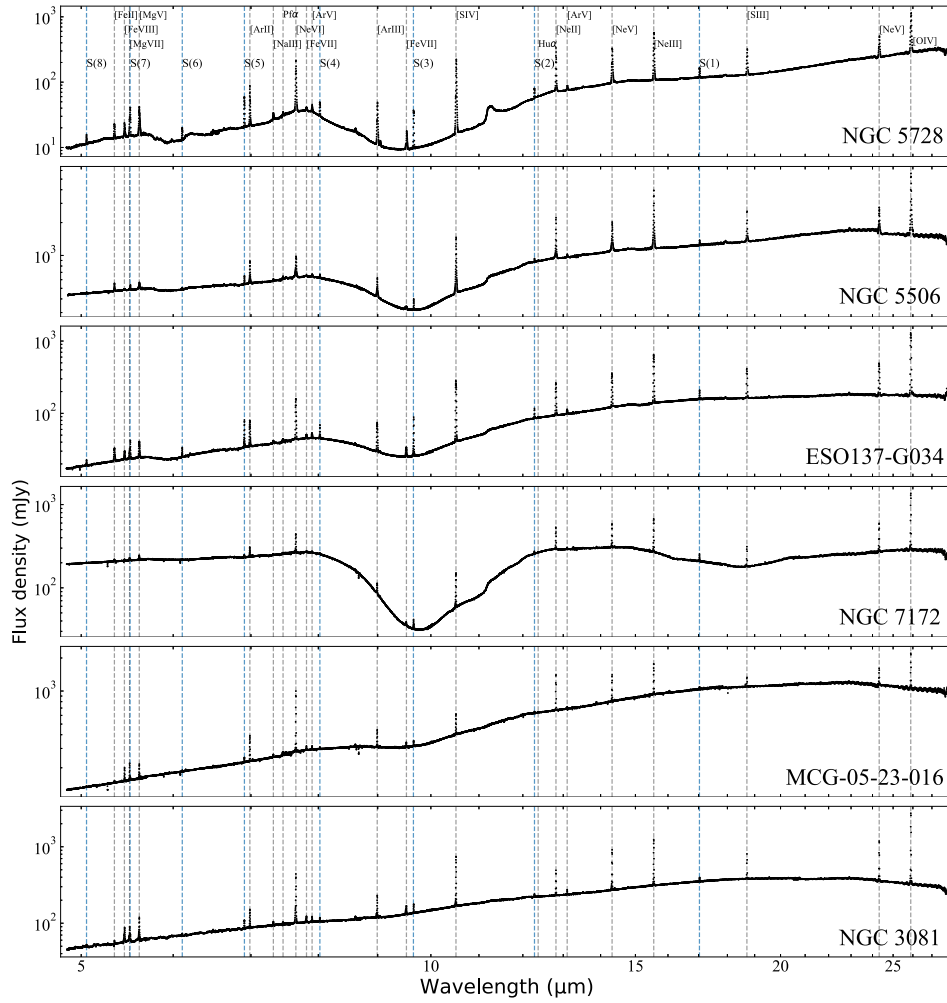
Figure 3. Mid-IR spectra extracted from the central $r = 0''\!.75$ aperture (centered on the continuum peak) for each sampled Seyfert galaxy, where 21 prominent ionized and 8 molecular lines as listed in Table 3 are marked in the top panel (zoom in to see more details).

AGN ionization cones in NGC 5728, NGC 5506, NGC 3081, and likely in ESO137-G034, and (2) find some intriguing highly disturbed regions perpendicular to their AGN ionization cones in NGC 5728, NGC 5506, and ESO137-G034. In addition, we find that NGC 7172 and MCG-05-23-016 also display the evidence of outflows, especially along the direction of their AGN ionization cones.

3.2.1. Flux Distributions

Figures 5(a1), (b1)–10(a1), (b1) present, using [Ne II] and [Ne V] lines as examples, distributions of the total flux (i.e., the integral of the best-fit emission line profile for each spaxel, denoted as f_{total} hereafter) of these six lines (Figures C1–C16).[33] Specifically, emission lines with relatively low ionization potentials (e.g., [Ar II], [Ne II]) exhibit more extended f_{total} distributions with more substructures. Meanwhile, emission lines with higher ionization potentials (e.g., [Ne V]) tend to exhibit more concentrated f_{total} distributions with certain

orientation dependence. This behavior is similar for all targets except for MCG-05-23-016, which only exhibits slight extension along the AGN ionization axis (as measured below) for all six lines. See Figures C1–C16 in Appendix C for f_{total} distributions of all six lines panel by panel and ordered according to their ionization potentials.

Different excitation sources are able to explain these different flux distributions (e.g., Sajina et al. 2022). Specifically, both the star formation and AGN activity can contribute to the excitation of relatively low ionization lines. Consistent with this, the f_{total} distributions of low ionization lines (e.g., [Ar II], [Ne II]) exhibit some extended structures, following the distributions of star-forming cold molecular gas traced by CO emission (gray dashed contours in Figures 5(a1)–10(a1)). Figures 5(a1)–10(a1) also exhibit that AGN ionization contributes to these low ionization lines around the nucleus as well, and we will discuss this again in Section 3.2.2. Meanwhile, for high ionization lines (e.g., [Ne V]), AGN ionization with a certain orientation dependence dominates their excitation as star formation activity cannot generate such high energy photons (~100 eV).

As indicated by black dashed lines in Figures 5(b1)–10(b1), the AGN ionization axis of each target is measured as the major axis of a elliptical source detected from [Ne V] f_{total} maps using `Source Extractor` (Bertin & Arnouts 1996; Barbary et al. 2017). Note

---

[33] Among these six emission lines, [Ne V] line has the highest (97.1 eV) ionization potential, while [Ne II] line has the lowest ionization potential (21.6 eV) except for [Ar II] line (15.8 eV). [Ne II] line is used for the illustration here and hereafter as this line is in the MRS subchannel with a field of view that is much larger than the one of [Ar II] line and is also more comparable to the one of [Ne V] line.
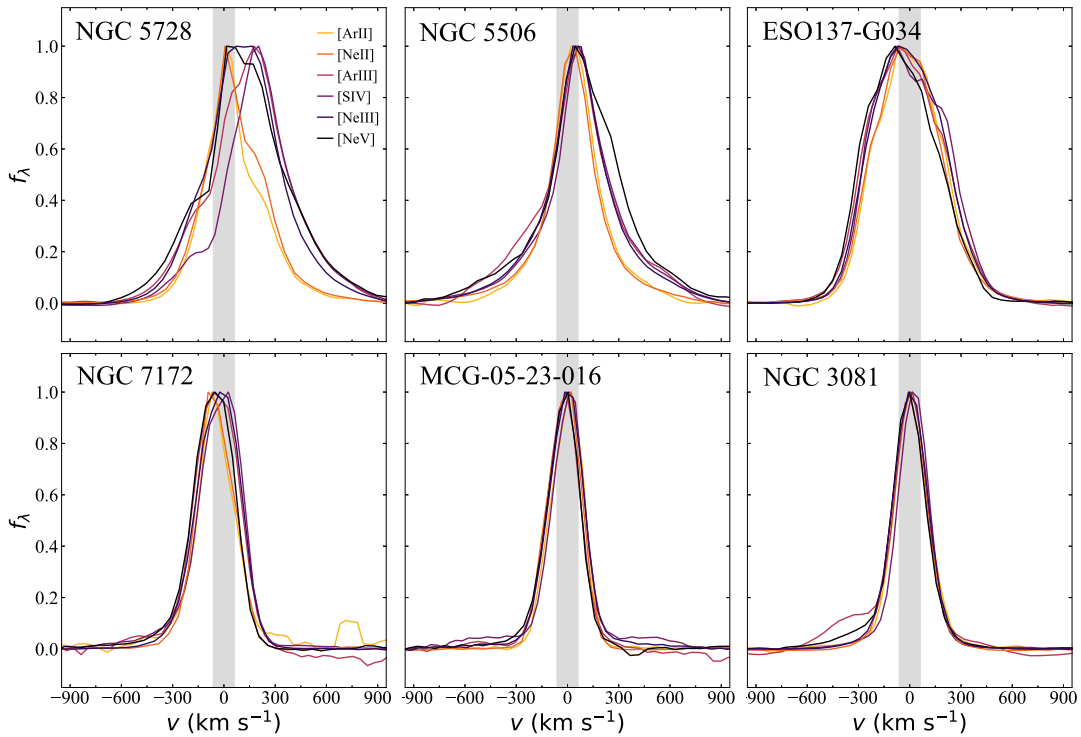
Figure 4. Normalized profiles of [Ar II] 6.985 μm, [Ne II] 12.814 μm, [Ar III] 8.991 μm, [S IV] 10.511 μm, [Ne III] 15.555 μm, and [Ne V] 14.322 μm emission lines from spectra in Figure 3, with the darker color indicating the higher ionization potential. The gray-shaded region in each panel indicates the FWHM of the instrumental broadening at the wavelength of [Ne III], which is the largest among the six lines. Note that these line profiles are in the rest frame converted according to the redshift listed in Table 1.

that the AGN ionization axis measured here of each target is basically aligned with their AGN ionization cone determined by optical emission lines (e.g., Fischer et al. 2013; Thomas et al. 2017; Shimizu et al. 2019; Ruschel-Dutra et al. 2021; Esposito et al. 2024), and/or radio jets (see gray dashed contours in Figures 5(b1)–10(b1); and, e.g., Morganti et al. 1999; Nagar et al. 1999; Thean et al. 2000; Orienti & Prieto 2010; Durré & Mould 2018 for the radio emission maps). AGN ionization cones are in general accompanied by outflows (e.g., King & Pounds 2015; Harrison & Ramos Almeida 2024), as is further discussed in the following subsection for our six targets.

3.2.2. Velocity Fields

In addition to the flux distribution, the velocity field also helps reveal the physical condition of ionized gas and the existence of ionized gas outflow in each target. Figures 5(a2), (b2)–10(a2), (b2) present the v_m distributions of [Ne II] and [Ne V] emission lines for the central region of each target (see Figures C2–C17 for complete v_m distributions of the six lines). As aforementioned, the v_m distribution traces the primary velocity field of each emission line.

For the six targets, their v_m distributions of low ionization lines (e.g., [Ar II], [Ne II]) all exhibit regular patterns, each with approximately centrally symmetric approaching and receding sides aligned with the kinematic major axis of the rotating gas disk (i.e., gray dashed lines in middle panels of Figures 5–10; and see references in their captions). Such v_m distributions indicate disk-rotation-dominated motions of low ionization lines. The v_m distributions of AGN ionization dominated high ionization lines, e.g., [Ne V], are all different from those of low ionization lines, with some of them even showing obvious

twists of their kinematic axes (see Figures 5(a2), (b2)–10(a2), (b2)). Such twisting is more significant for NGC 5728, NGC 5506, NGC 3081, and slight for ESO137-G034 (see further note on ESO137-G034 at the end of this subsection), while the v_m distributions of high ionization lines in NGC 7172 and MCG-05-23-016 exhibit more perturbations. The contrasting v_m distributions highlight that emission lines of different ionization potentials are tracing different gas motions.

The kinematic major axes of the v_m distributions for [Ne V] emission line, as the representative of high ionization lines, tend to be aligned with the AGN ionization cones (i.e., black dashed lines in Figures 5(a1) and (b1)–10(a1) and (b1)). This trend is also more significant for NGC 5728, NGC 5506, NGC 3081, and ESO137-G034 (see Figures 5(b2)–7(b2), and 10(b2)). For their v_m distributions, the kinematic major axis gradually twists from those of [Ar II] and [Ne II] to that of [Ne V] with an angle ranging from ∼45° to 90° (see Figures C2, C5, C8, and C17 for the more complete trend of such twisting in these four targets). Given the consistent orientations of the [Ne V] v_m distributions and the AGN ionization cones, a reasonable explanation for such twisting of these targets is the increasing contribution of AGN-driven outflows in the primary motion of ionized gas. Namely, while v_m distributions of low ionization lines (e.g., [Ar II], [Ne II]) trace disk-rotation motions, v_m distributions of high ionization lines (e.g., [Ne V]) are increasingly dominated by outflow motions along the AGN ionization cone.

More importantly, for NGC 5728, NGC 5506, ESO137-G034, and NGC 3081, their velocity distributions of the relatively broader components (i.e., $v_{comp.\ 2}$), which are in general purely contributed by gas outflows, in [Ne II] and [Ne V] emission lines are also aligned with the AGN ionization cones (see Figures 11–14 and the brief discussion in
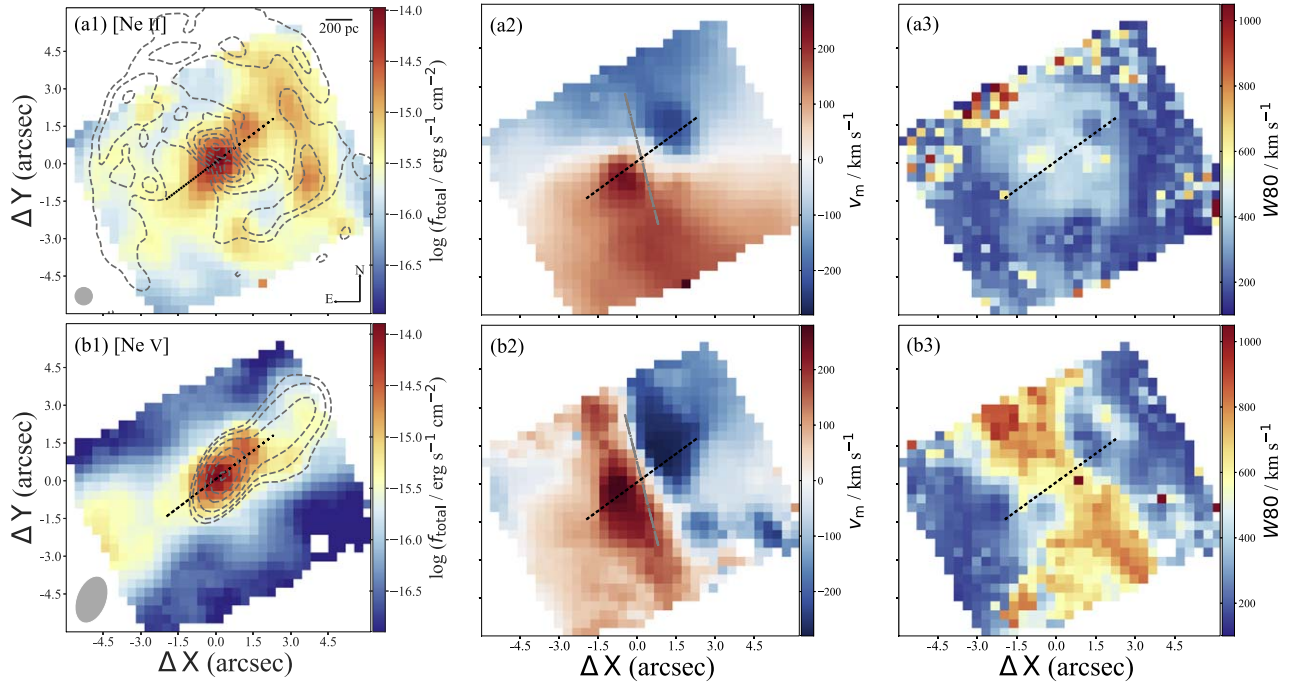
Figure 5. The distributions in NGC 5728 central region for f_{total} (left panels), v_m (middle panels), and W_{80} (right panels) of [Ne II] 12.814 μm (top) and [Ne V] 14.322 μm (bottom) emission lines. For all panels, the origin of coordinates is on the infrared continuum peak as location of the AGN. Panel (a1) also features a filled gray circle to indicate the angular resolution (i.e., $0\rlap{.}{''}7 \times 0\rlap{.}{''}7$) of all colored maps, a compass (with N is up, and E is to the left), and a scale bar of 200 pc; they are the same for other panels in this figure. The gray dashed contours in panel (a1) indicate the Atacama Large Millimeter/submillimeter Array CO(2-1) emission map as in Figure 1. The CO emission map here and hereafter is, unless specifically noted, convolved to the same angular resolution as the emission line maps, from 0.075, 0.15, 0.3, 0.5, 0.7, to 0.95 of the peak CO intensity. The gray dashed contours in panel (b1) indicate the Very Large Array 4.9 GHz (6 cm) radio emission map (see acknowledgments), from 0.15, 0.2, 0.3, 0.5, 0.7, to 0.975 of the peak radio intensity unless specifically noted, with the gray ellipse indicating the beam size of the radio map. The black dashed line in each panel indicates the measured AGN ionization axis with the position angle (PA) of 127°(see Section 3.2.1). The gray dotted–dashed lines in panels (a2), (b2) indicate the kinematic major axis of the rotating gas disk in NGC 5728 with the PA of 194°, which is fitted from CO(2-1) velocity field by Shimizu et al. (2019).

Appendix A). Moreover, their v_m distributions of the [Ne V] emission line are qualitatively similar to these velocity distributions of the relatively broader components in [Ne II] and [Ne V] emission lines. This result supports the explanation that the twisting between the v_m distributions of different emission lines in the four targets is due to the increasing contribution of AGN-driven outflows in the primary motion of ionized gas. Under such situation, the low outflow strengths of NGC 7172 and MCG-05-23-016 are able to explain the lacking of significant twisting of their [Ne V] v_m distributions against those of [Ne II], as such twisting is intrinsically because of collimating motions of highly ionized gas in strong outflows.

Although NGC 7172 and MCG-05-23-016 do not clearly exhibit such twisting between v_m distributions of different emission lines, they still display the evidence of outflows around their AGN. The observed MIR emission line ratios along with theoretical calculations indicate the existence of fast radiative shocks ($v \approx 100$–$1000 \, km \, s^{-1}$) associated with outflows in NGC 7172 and MCG-05-23-016 (Hermosa Muñoz et al. 2024a; Zhang et al. 2024). As further checked in Figure 15, the evidence of fast radiative shocks is still there for individual spaxels within the central region of NGC 7172 and MCG-05-23-016. This result is more evident for spaxels located along the direction of their AGN ionization axes (i.e., the reddish and yellowish points in Figure 15). Namely, while the signature of relatively stronger collimating outflows (i.e., the twisting of velocity fields) in NGC 7172 and MCG-05-23-016 is lacking, these two targets still exhibit the evidence of outflows along their AGN ionization axes given the existence of fast radiative shocks. For the other four targets, we

have checked that while some spaxels in the periphery, especially for NGC 3081, exhibit characteristics of fast radiative shocks, their central regions are dominated by the AGN excitation, especially for ESO137-G034.

Furthermore, with the same JWST/MRS data set, Hermosa Muñoz et al. (2024a) and Esparza-Arredondo et al. (2024) provide more specific studies for NGC 7172 and MCG-05-23-016, respectively. Specifically, Hermosa Muñoz et al. (2024a) found from [Ne V] and [Ne VI] emission lines a biconical ionized gas outflow emerging N–S from the nucleus, extending at least $\sim 2\rlap{.}{''}5$ N and $3\rlap{.}{''}8$ S (projected distance of ~ 450 and 680 pc, respectively). Most of the emission arising in the northern part of the cone was not previously detected due to obscuration (e.g., Alonso-Herrero et al. 2023). Moreover, Hermosa Muñoz et al. (2024a) revealed that NGC 7172 is likely a case of weak coupling between outflow and the host given the kinematic properties and geometry of the outflow. This can further explain the lacking of significant collimating outflows along the AGN ionization axis in NGC 7172. Meanwhile, the intensity maps of [Ne V] and [Ne VI] emission lines of MCG-05-23-016 exhibit point-like distributions. Nevertheless, Esparza-Arredondo et al. (2024) observed clumps of more extended warm molecular gas traced by the H_2 $S(3)$, $S(4)$, and $S(5)$ lines with velocity dispersions of up to $\sim 160 \, km \, s^{-1}$, in regions where cold molecular gas traced by CO(2-1) emission is absent. They found one of these clumps, located at ~ 350 pc NW of the nucleus, shows kinematics that are consistent with outflowing gas, while this clump is more likely associated with star formation activity.
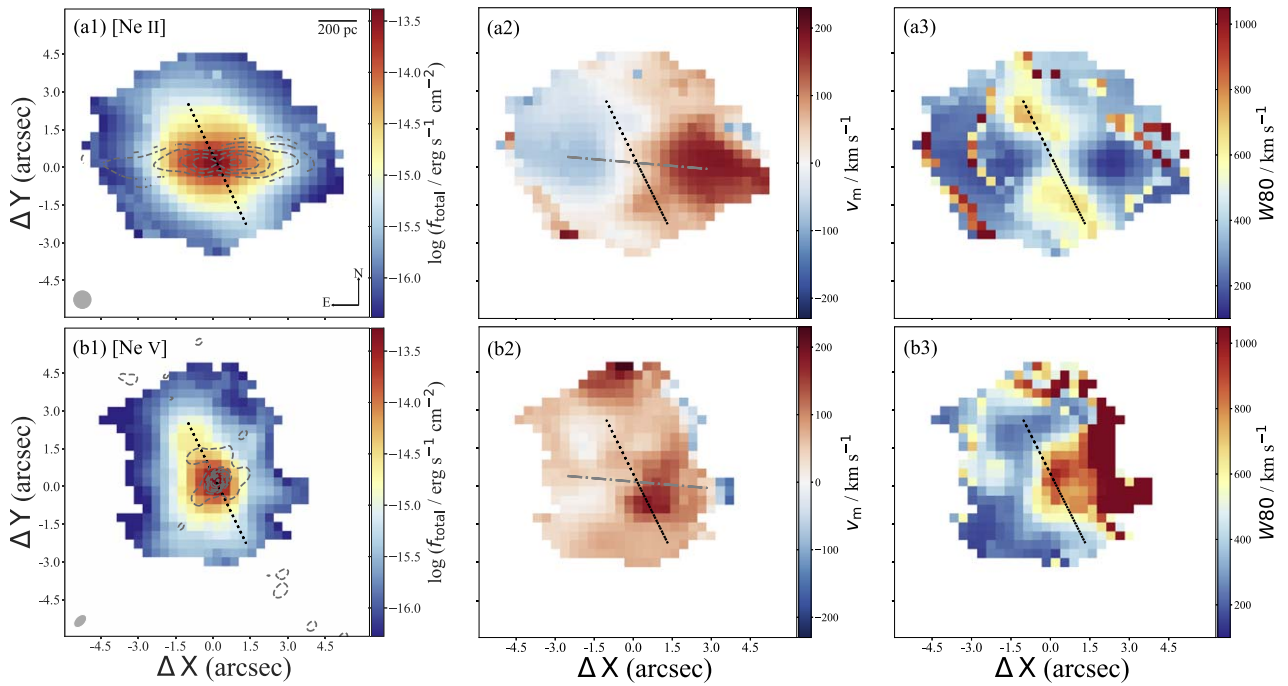
Figure 6. The same as Figure 5 but for NGC 5506. The contours of the Very Large Array 4.9 GHz radio emission map are from 0.01, 0.075, 0.15, 0.2, 0.3, 0.5, 0.7, to 0.975 of the peak radio intensity to highlight the diffuse wing-like radio emission. The PA of the measured AGN ionization axis (black dashed line in each panel) is 26°. The PA of the kinematic major axis (gray dotted–dashed lines in panels (a2) and (b2)) of the rotating gas disk in NGC 5506 is 265°, which is fitted from CO(3-2) data cube by Esposito et al. (2024).

In addition, Davies et al. (2024) provided a detailed discussion on the complex geometry of the circumnuclear region of NGC 5728 based on the data set presented here. They illustrated that the AGN ionization cone (as shown in Figure 5) and the corresponding gas outflow in NGC 5728 strongly intersect with the galaxy gas disk. In particular, most of the approaching side of the outflow cone lies behind the galactic disk while vice versa for the receding side. This kind of outflow geometry, especially the relatively perpendicular outflow orientation against the line of sight, is also reflected by the flux distributions and velocity fields of the relatively broader components in [Ne II] and [Ne V] emission lines (i.e., Figures 11–14), as well as the emission line profiles of the nuclear spectra (i.e., Figure 4). Consistent with such outflow geometry, these flux distributions and velocity fields, also the emission line profiles, exhibit comparable redshifted and blueshifted components, with even stronger redshifted contributions. Moreover, given the relatively low AGN luminosity of the six targets (i.e., $\sim 10^{43.4}$–$10^{44.3}$ erg s^{-1}) and hence the relatively low outflow strength (Fiore et al. 2017), the outflowing ionized gas in the six targets may not eventually escape the galaxy but may be decelerated by the galaxy gravity to stop and even fall back from certain radius (Alonso-Herrero et al. 2023; Davies et al. 2024; Esposito et al. 2024).

Note that the six targets are *selected* with prior outflow rate measurements to study how outflows are launched and driven from AGN with similar luminosities, but significantly different outflow strengths. Therefore, the existence of ionized gas outflows in all the six targets is within expectation, whereas the 100% detection rate of outflows is not applicable to a more general sample of AGN (e.g., Fischer et al. 2013; Förster Schreiber et al. 2019; Leung et al. 2019; Ruschel-Dutra et al. 2021). Some of our targets were also included in previous studies based on slit or IFU spectral observations in optical bands (e.g., Fischer et al. 2013; Ruschel-Dutra et al. 2021), while not all of these targets were claimed to

exhibit significant signatures of ionized gas outflows according to the different criteria in these studies. This result could be due to the mismatch between the slit position and the outflow cone (Fischer et al. 2013), or more likely due to the obscuration effect in optical bands as found by Hermosa Muñoz et al. (2024a). Accordingly, further study using JWST/MRS observations is promising to reveal relatively weak outflow signatures in different targets that might be missed by optical observations.

Among the four targets with velocity fields showing the evidence of ionized gas outflows, we further note the following points. The v_m distribution of [Ne II] emission line in NGC 5728 exhibits significant discrepancy against the kinematic major axis of the rotating gas disk around the AGN (see Figure 5(a2)). This is consistent with the argument in Section 3.2.1 that the AGN ionization (i.e., the corresponding outflow) contributes to these low ionization lines around the AGN as well (see also Shimizu et al. 2019; and Davies et al. 2024). The v_m distribution of [Ne V] emission line in NGC 5506 exhibits a complex outflow structure with the relatively weak blueshifted and strong redshifted components, as well as the redshifted velocity blob $\sim$600 pc toward the N. Such complex v_m distribution in NGC 5506, especially the redshifted velocity blob toward the N, can be attributed to the nearly perpendicular large-scale ionized gas outflows with the wide open angle as detailed by Esposito et al. (2024).[34] Specifically, Esposito et al. (2024) found consistent characteristics as shown here of the ionized gas kinematics in NGC 5506 based on Gran Telescopio CANARIAS (GTC)/ MEGARA IFU observations. Further detailed study of NGC 5506 and also NGC 3081 in this series will be presented by D. Delaney et al. (2024, in preparation).

---

[34] Esposito et al. (2024) also found some blueshifted blobs in the S of the velocity field of the broad component in [O III] emission line, but these blobs are out of the field of view of the data set studied here.
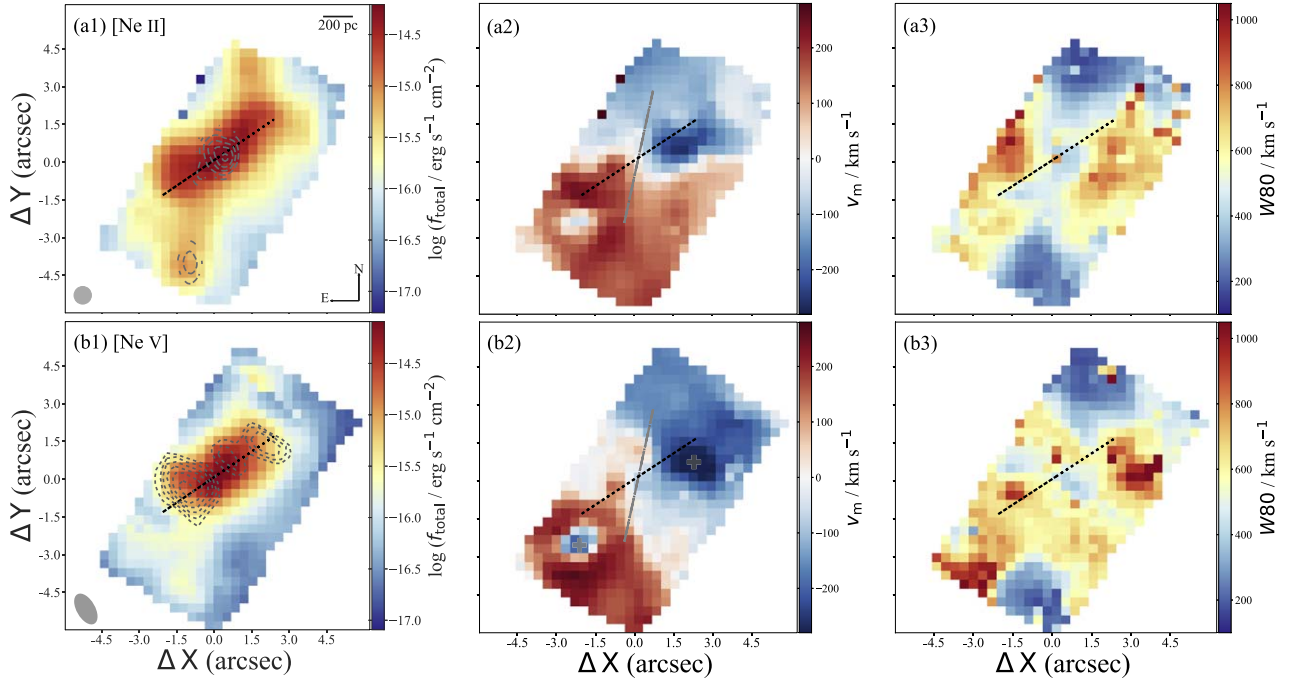
Figure 7. The same as Figure 5 but for ESO137-G034. The gray dashed contours in panel (b1) indicate 8.6 GHz (3.5 cm) radio emission map extracted from Morganti et al. (1999). The observation is taken by the Australia Telescope Compact Array, and the contours are from -0.5, -0.4, 0.4, 0.5, 0.7, 1, 1.3, to 1.8 mJy beam^{-1}. The PA of the measured AGN ionization axis (black dashed line in each panel) is $124°$. The PA of the kinematic major axis (gray dotted–dashed lines in panels (a2) and (b2)) of the rotating gas disk is $168°$, which is measured from the v_m distribution of [Ne II] emission line in panel (a2) after masking the two kinematically distinct regions as marked by gray plus signs in panel (b2) (see the method in Krajnović et al. 2006).
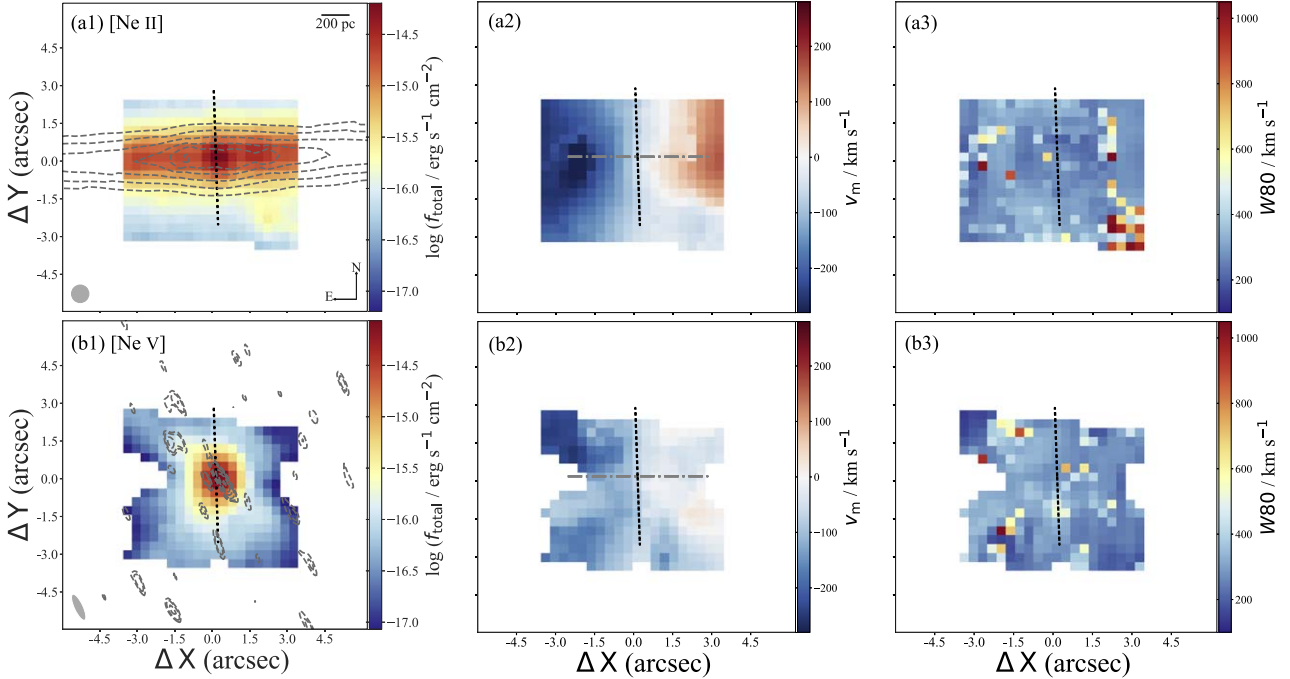
Figure 8. The same as Figure 5 but for NGC 7172. The CO(2-1) emission map here has a little worse angular resolution comparing with the emission line maps, and hence, no convolution of the CO emission map is performed. The PA of the measured AGN ionization axis (black dashed line in each panel) is $2°$. The PA of the kinematic major axis (gray dotted–dashed lines in panels (a2) and (b2)) of the rotating gas disk in NGC 7172 is $270°$, which is fitted from CO(3-2) data cube by Alonso-Herrero et al. (2023).

Additionally, the v_m distributions of ESO137-G034 all exhibit two significant kinematically distinct regions (KDRs) $\sim$400 pc toward the SE and NW, respectively (see Figures 7(a2), (b2), and C8). These KDRs severely affect the decomposition of the broad components associated with

outflows in [Ne II] and [Ne V] emission lines. Thus, the broad components in [Ne II] and [Ne V] emission lines cannot be clearly associated to ionized gas outflows (see Figure 13). Further detailed study of ESO137-G034 in this series will be presented by H. Haidar et al. (2024, in preparation).
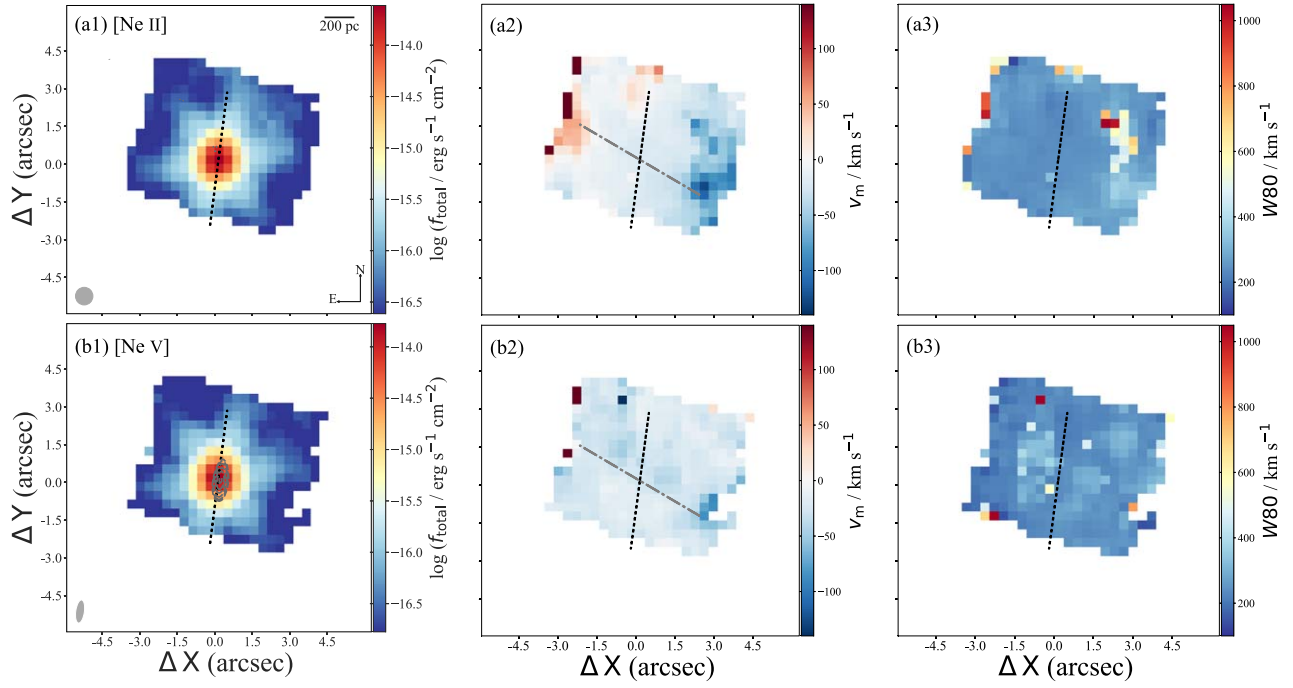
Figure 9. The same as Figure 5 but for MCG-05-23-016. The PA of the measured AGN ionization axis (black dashed line in each panel) is 172°. The PA of the kinematic major axis (gray dotted–dashed lines in panels (a2) and (b2)) of the rotating gas disk in MCG-05-23-016 is 59°, which is fitted from CO(2-1) data cube by Esparza-Arredondo et al. (2024).
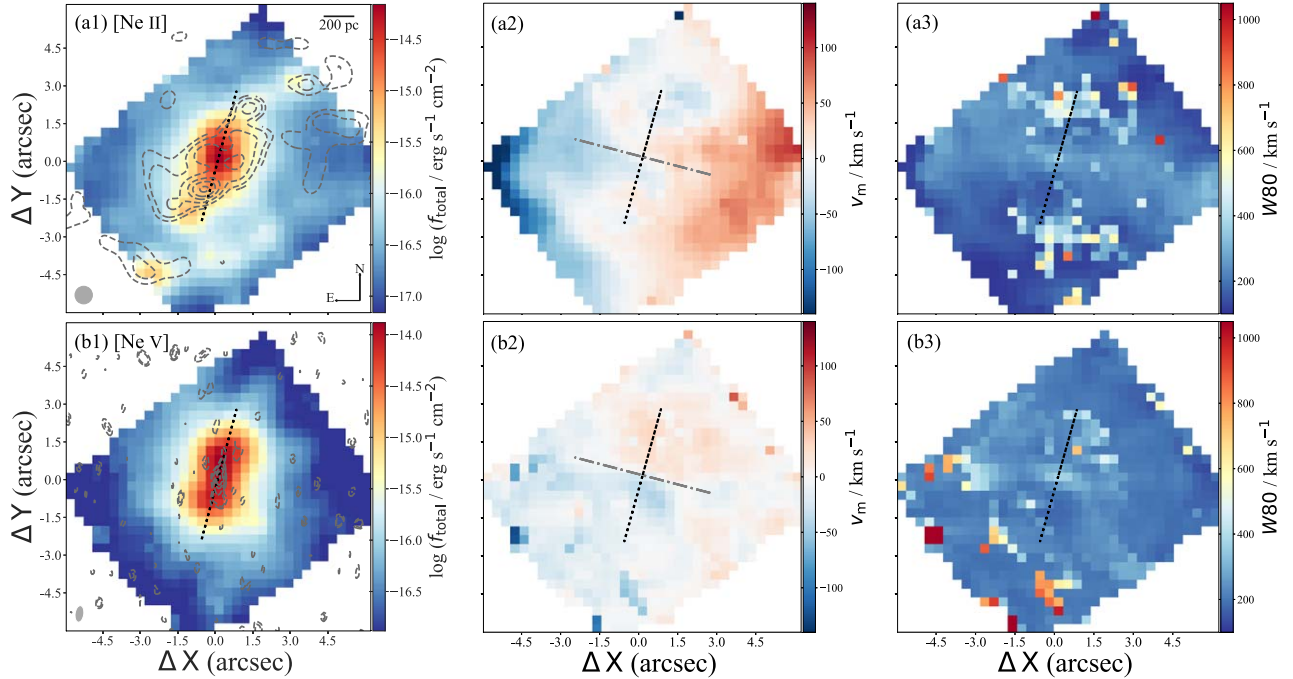
Figure 10. The same as Figure 5 but for NGC 3081. The PA of the measured AGN ionization axis (black dashed line in each panel) is 165°. The PA of the kinematic major axis (gray dotted–dashed lines in panels (a2) and (b2)) of rotating gas disk is 255°, which is fitted from [N II] velocity field by Ruschel-Dutra et al. (2021).

3.2.3. W80 Maps

Among the six targets, we find NGC 5728, NGC 5506, and ESO137-G034 exhibit widely distributed regions of significantly broadened [Ne V] emission line (Figures 5(a3), (b3)–7(a3), (b3), and see also Figures C3–C9). The other three targets do not exhibit such spatially extended regions of large W_{80}, but have some discrete spaxels with large W_{80} values

within the field of view (Figures 8(a3), (b3)–10(a3), (b3), and see also Figures C12–C18). This result is consistent with the relatively broader emission line profiles of the former three targets as discussed in Section 3.1. For convenience of discussion here and in Section 4, we simply denote the regions with $W_{80} > 600\,\mathrm{km\,s^{-1}}$ as the "highly disturbed regions" (e.g., Sun et al. 2017; Kakkad et al. 2020; Ruschel-Dutra et al. 2021).
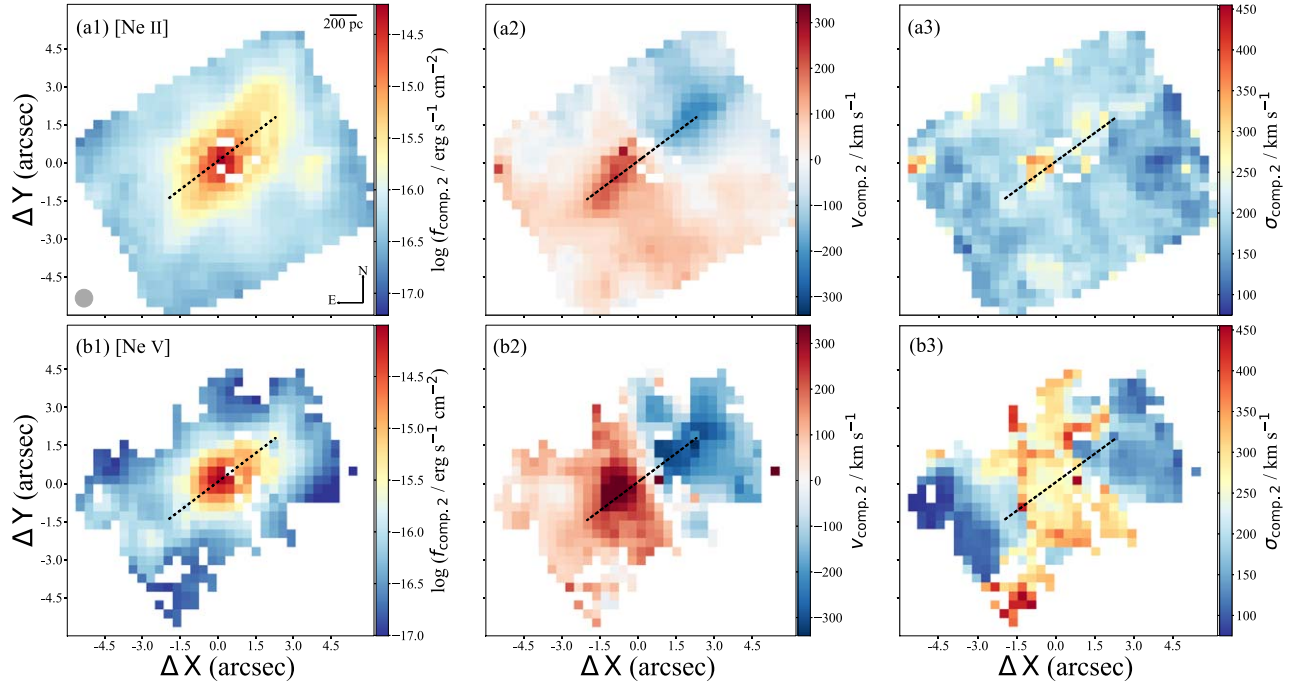
Figure 11. The distributions in NGC 5728 central region for flux (left panels), velocity (middle panels), and velocity dispersion (right panels) of [Ne II] 12.814 μm (top) and [Ne V] 14.322 μm (bottom) emission lines. The black dashed line in each panel indicates the measured PA of the AGN ionization axis. Panel (a1) also features a filled gray circle to indicate the angular resolution (i.e., $0''7 \times 0''7$) of all colored maps, a compass (with N is up, and E is to the left), and a scale bar of 200 pc; they are the same for other panels in this figure.
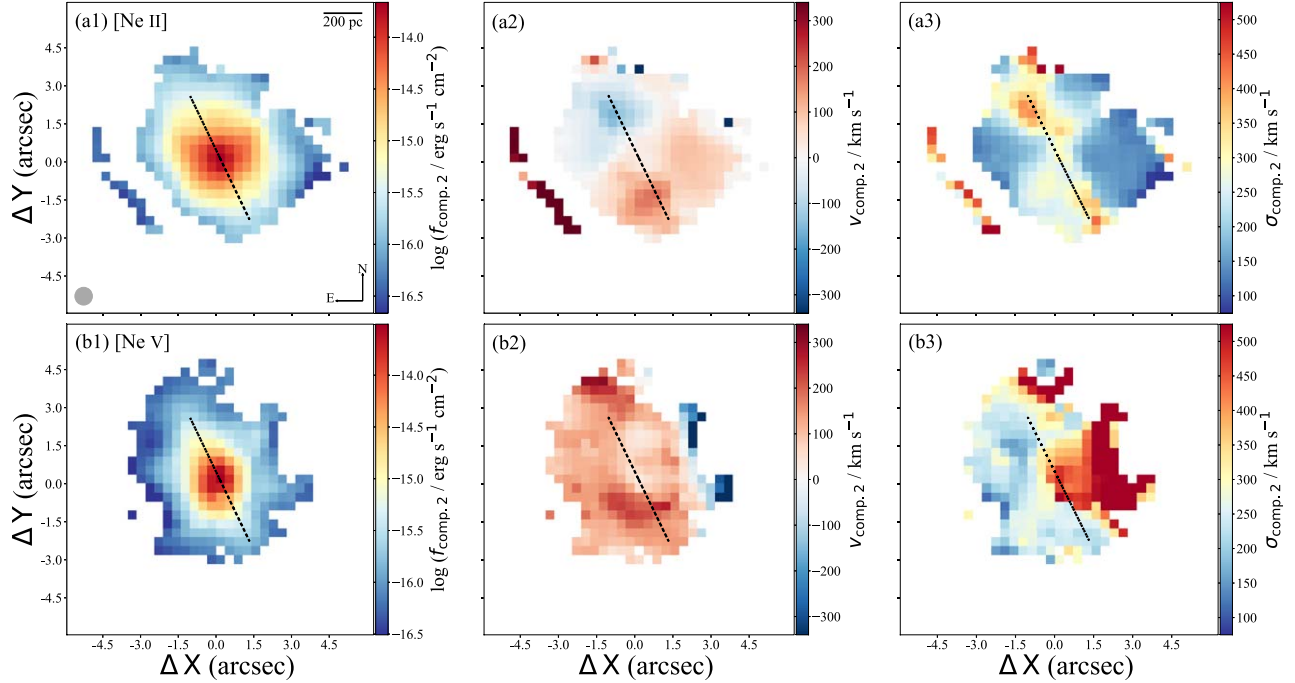
Figure 12. The same as Figure 11 but for NGC 5506.

Besides the large values, the W_{80} distributions of NGC 5728, NGC 5506, and ESO137-G034 also exhibit some intriguing features (see also García-Bernete et al. 2024c; Davies et al. 2024). Specifically, their W_{80} distributions of the [Ne V] emission line show that the highly disturbed regions in NGC 5728 and NGC 5506 are not aligned with their AGN ionization axes, and hence not aligned with the ionized gas outflows discussed in Section 3.2.2, but approximately perpendicular to them. For ESO137-G034, the W_{80} distribution of the [Ne V] emission line is even more intriguing. The highly disturbed regions in ESO137-G034 are primarily aligned with the AGN ionization axis, while they also exhibit some minor components roughly perpendicular to the AGN ionization axis. Furthermore, while the highly disturbed regions in NGC 5728 and NGC 5506 essentially stretch across their AGN, those of ESO137-G034 are located away from the AGN.
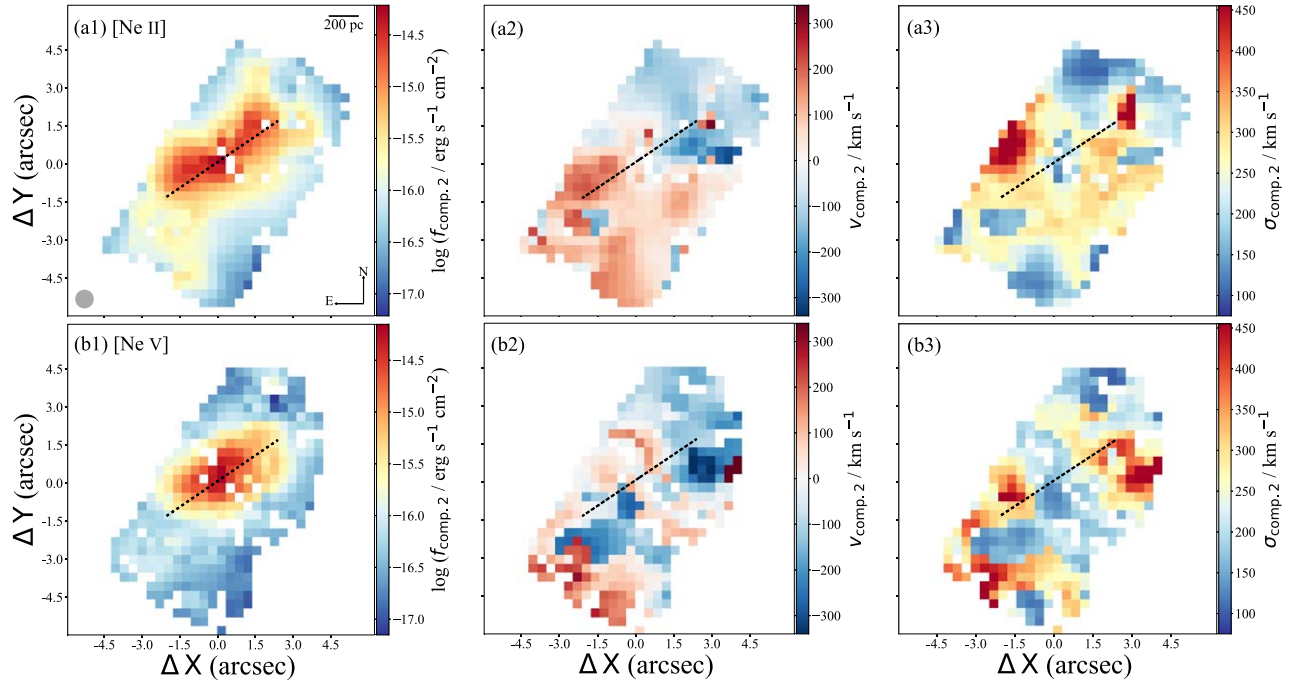
Figure 13. The same as Figure 11 but for ESO137-G034. Note that velocity and velocity dispersion fields in panel (b2) and (b3) are more disturbed around the KDRs comparing with v_m and W_{80} distributions of [Ne V] emission line as shown in Figures 7(b2), (b3).
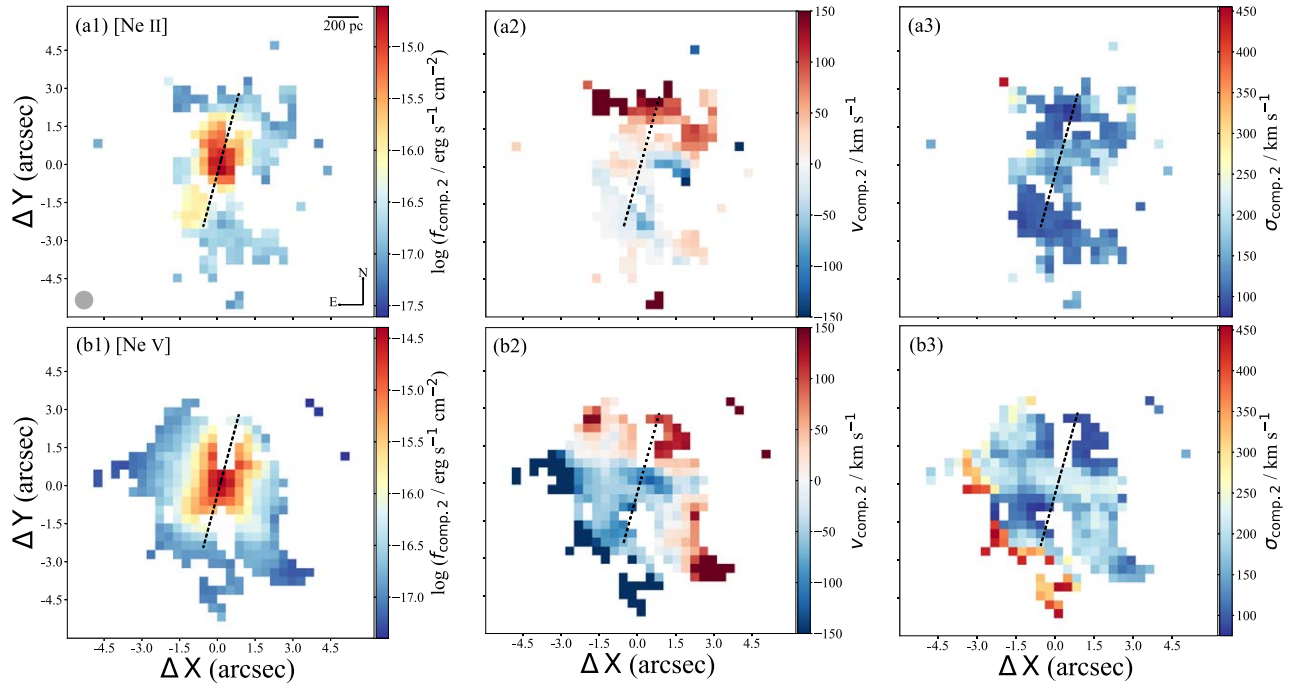
Figure 14. The same as Figure 11 but for NGC 3081.

4. Highly Disturbed Regions and the Triggering Mechanism

Section 3.2.3 has shown that NGC 5728, NGC 5506, and ESO137-G034 have intriguing highly disturbed regions. Here, we further discuss the nature of these disturbed regions. Figure 16 presents AGN excitation strength distributions using the [Ne V]/[Ne II] line ratio as the indicator (e.g., Genzel et al. 1998; Dale et al. 2006; Armus et al. 2007), to disentangle the spatial correlation between these regions and AGN activities. For

NGC 5728 and NGC 5506, the most highly disturbed regions, i.e., the gray-shaded areas in Figure 16, are approximately perpendicular to their AGN ionization cones (i.e., reddish areas), while that is not the case for ESO137-G034.

4.1. Highly Disturbed Regions in NGC 5728

The highly disturbed regions in NGC 5728 could be attributed to outflows launched with an angle to the galaxy disk (Ruschel-Dutra et al. 2021). However, in Section 3.2.2, we
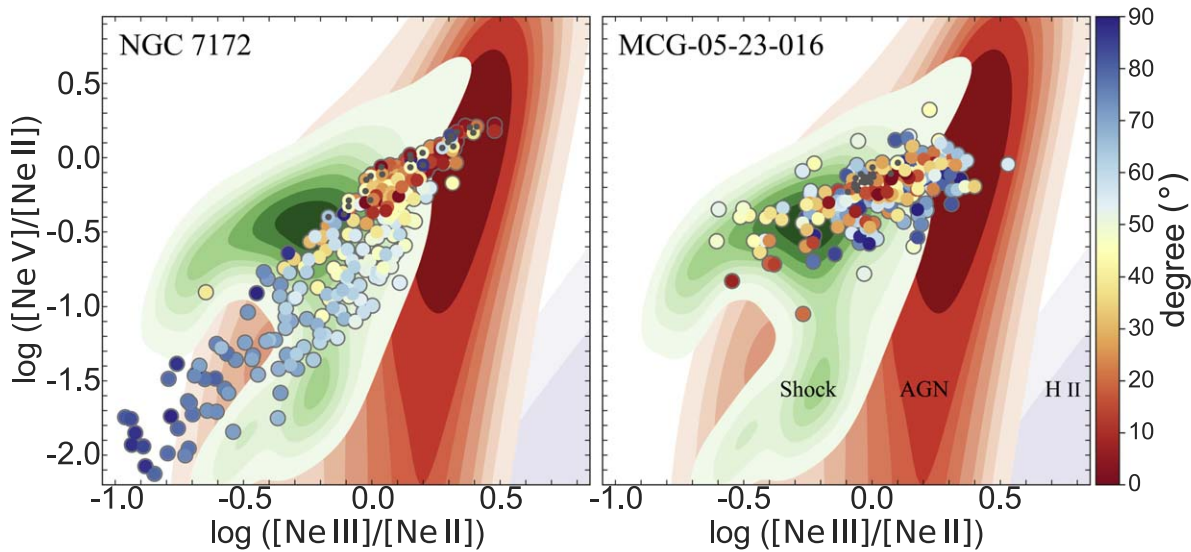
Figure 15. The diagnostic diagram of ionized emission line ratios [Ne V]/[Ne II] vs. [Ne III]/[Ne II] for spatially resolved spaxels in NGC 7172 (left) and MCG-05-23-016 (right), color coded according to the orientation of each spaxel relative to the AGN ionization axis (0° and 90° mean parallel and perpendicular to the AGN ionization axis, respectively). The data points with a gray dot pertain to spaxels within the central $r = 1''$ aperture. The greenish, reddish, and purplish contours (from the left to the right) in each panel are the model results for fast radiative shocks, AGN, and H II regions, respectively. The fast radiative shock models ($v \approx 100$–1000 km s^{-1}; including the shock precursor) are calculated using the MAPPINGS V (Sutherland & Dopita 2017) by Alarie & Morisset (2019), while the H II and AGN models are calculated using CLOUDY (Ferland et al. 2017; Chatzikos et al. 2023) by Morisset et al. (2015) and Pereira-Santaella et al. (2024), respectively.
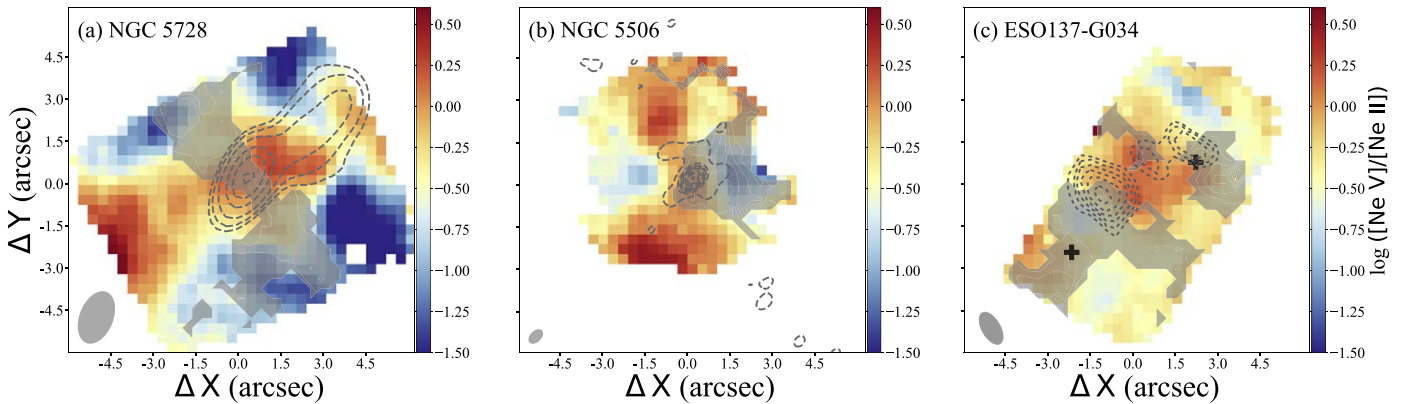
Figure 16. [Ne V]/[Ne II] line ratio distributions as the indicator of AGN excitation strength for central regions of (a) NGC 5728, (b) NGC 5506, and (c) ESO137-G034. In each panel, the dashed contours indicate the radio emission as in Figures 5(b1), 6(b1), and 7(b1), while the gray-shaded areas delineate the subregion with $W_{80} > 600$ km s^{-1} measured for the [Ne V] emission line (Section 3.2.3). For NGC 5728 in panel (a), Very Large Array (VLA) image at 4.9 GHz revealed an elongated nuclear radio jet along the AGN ionization cone (Durré & Mould 2018). For NGC 5506 in panel (b), VLA images at 4.9 and 8.5 GHz exhibit an unresolved nuclear core and diffuse wing-like radio emission extending mainly to the NW and E of the AGN (Orienti & Prieto 2010). For ESO137-G034 in panel (c), The Australia Telescope Compact Array image at 8.6 GHz exhibits two off-nuclear radio blobs toward SE and NW (Morganti et al. 1999). Additionally, the black plus signs in panel (c) indicate two kinematically distinct regions as in Figure 7(b2).

reveal that the ionized gas outflow around the AGN in NGC 5728 is mainly aligned with the AGN ionization cone, and for the case of NGC 5728 is almost within the galaxy disk (Shimizu et al. 2019; Davies et al. 2024). The perturbations induced by central accreting flows might also contribute to these highly disturbed regions since these regions are aligned with the accretion disk plane. Specific kinematic modeling is required to ascertain whether this is the case.

Very recent studies have reported AGN with low-power ($\lesssim 10^{44}$ erg s^{-1}) radio jets, as is the case here, generally result in intense and extended velocity dispersions perpendicular to the radio jets and hence the ionization cones (e.g., Venturi et al. 2021, 2023; Audibert et al. 2023; Peralta de Arriba et al. 2023; Hermosa Muñoz et al. 2024b; Speranza et al. 2024; Ulivi et al. 2024). According to

simulations, this kind of perpendicular disturbed region is due to the more dramatic jet–interstellar matter (ISM) interaction occurring in AGN with the low-power jets (Mukherjee et al. 2018a, 2018b; Meenakshi et al. 2022).

Specifically, the strongly interacting propagation of the low-power radio jet through the gas disk will result in significant shocks and dispersions, as well as outflows and the trigger of star formation (Nyland et al. 2018). These processes will strongly disturb the gas disk, especially in the direction perpendicular to the jet, where has minor resistance. Consistent with this scenario, Figure 17 provides a phenomenological model for the potential outflow structure in NGC 5728. This model contains a nuclear radio jet that indirectly drives outflows along the AGN ionization cone, along with shock-driven highly disturbed regions that are
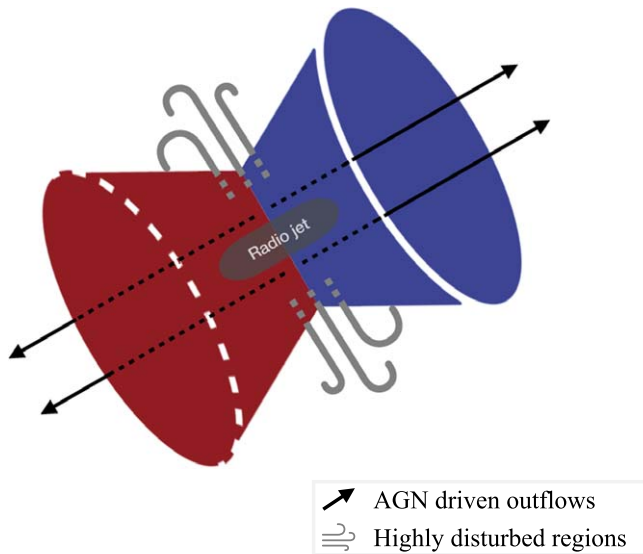
Figure 17. Schematic diagram for the phenomenological model to illustrate AGN driven outflows indicated by black arrows along the AGN ionization cone, and highly disturbed regions indicated by gray curves perpendicular to the AGN ionization cone. The approaching and receding sides of the AGN ionization cone are sketched in blue and red, respectively.

perpendicular to the AGN ionization cone. Note that this model is only for a phenomenological explanation, while a conclusive explanation requires specific modeling and/or simulations beyond the scope of this work.

4.2. Highly Disturbed Regions in NGC 5506

The situation is more complicated for NGC 5506, which contains an unresolved radio core and diffuse wing-like radio emission bisected by the AGN ionization axis. The asymmetry of the highly disturbed regions in NGC 5506 is likely due to the edge-on view and the asymmetric radio emission. As shown in Figure 6(b2) (see also Figure C5), the blueish NE side, which is more obvious in the [Ne II] $v_{comp. 2}$ field (see Figure 12(a2)), represents the approaching side of the AGN ionization cone in NGC 5506. This geometry explains why the diffuse wing-like radio emission in NGC 5506 was observed extending mainly to the NW and E of the nucleus, as these directions are intrinsically toward us.

We can then still use the model in Figure 17 to illustrate the potential outflow structure in NGC 5506, but viewing the phenomenological model from the right to the left, and imagining there is a horizontal gas disk with the near side slightly tilted toward the S (Fischer et al. 2013). As a consequence, we can see asymmetrical highly disturbed regions toward the E and the N that are above the tilted gas disk of NGC 5506 (see Figure 6(b3)), while disturbed regions toward the W and the S are blocked by the gas disk. When scrutinizing Figure 6(b3), we find a few spaxels in the E exhibit lager W_{80} values as well, which are plausibly associated with the blocked disturbed regions.

4.3. Highly Disturbed Regions in ESO137-G034

Since the highly disturbed regions in ESO137-G034 are located away from the AGN, their triggering mechanism could be associated with some "delayed" feedback effects rather than a recent episode of AGN activity. Specifically, we hypothesize the AGN activity in ESO137-G034 triggered the off-nuclear radio blobs first, which then interacted with the ISM gas and increased the gas dispersion as they propagated. Moreover, the

propagation of those radio blobs is expected to result in these KDRs on the radio front via enhanced perturbations in the KDR vicinity. In this situation, the phenomenological model in Figure 17 is still applicable to ESO137-G034, where the minor components of highly disturbed regions perpendicular to the AGN ionization are similar to the highly disturbed regions in NGC 5728 and NGC 5506, but already in the fading phase. Again, the analysis here is only for a phenomenological explanation, while a more conclusive explanation requires specific modelings and/or simulations.

4.4. Discussion

Within these highly disturbed regions, some spaxels exhibit the [Ne V] emission line of double-peaked line profiles having comparable blueshifted and redshifted components. This is also why we adopt the nonparametric methodology for the analysis. In principle, a mixed motion of the outflowing component and the rotating disk could result in such double-peaked profiles as well. However, this scenario should not be the case here as detailed below.

For NGC 5728, NGC 5506, ESO137-G034, and NGC 3081, the [Ne V] kinematics tend to be dominated by AGN-driven outflowing motions (Section 3.2.2). As for the [Ne V] broad component, we also checked the velocity fields of the [Ne V] narrow component from the double-Gaussian fitting results for these targets. We find for these targets that the velocity fields of the [Ne V] narrow component exhibit basically the same orientations as the corresponding v_m fields of [Ne V] emission line as well, and are different from v_m fields of the [Ne II] emission line. This result supports that the [Ne V] kinematics in these targets are dominated by outflows, and the double-peaked profile should be due to mixed outflows in these highly disturbed regions along and against our light of sight (e.g., Fischer et al. 2011; Bae & Woo 2016). The case of ESO137-G034 is more complicated given the existence of the KDRs, and will be further discussed by H. Haidar et al. (2024, in preparation).

Furthermore, these highly disturbed regions in NGC 5728 and NGC 5506 are aligned with the zero-velocity demarcations, i.e., the kinematic minor axis, of their [Ne V] v_m fields as well. This invokes another concern that for galaxies with a large central velocity gradient, when averaging out in one resolution element, two opposite streams in velocity will also result in an apparent large velocity dispersion. Nevertheless, given the above discussion, such a large central velocity gradient, if it exists, can only come from outflow motions. Namely, no matter whether they are disturbed or not, these widely distributed regions that are perpendicular to the AGN axis should be associated with outflow relevant processes, albeit they do not mean the outflow itself.

5. Quantification of the Outflow Strength

In Section 3.2.2, we showcase the evidence of ionized gas outflows in the six targets. In this section, we provide a rather quantitative comparison of the outflow strength among the six targets.

The most widely used outflow rate is the integrated outflow rate measured from an aperture while assuming a specific outflow geometry. We first estimate for each target a rough upper limit of the integrated ionized gas outflow rate from a $r = 0\rlap{.}''9$ aperture (the same as in Davies et al. 2020b). These upper limits take the ionized gas mass derived from the total [Ne V] 14.322 μm flux of all spaxels within the circular aperture

Table 4
Integrated Ionized Gas Outflow Rates

Galaxy (1)	$\log \frac{n(\mathrm{Ne}^{4+})}{n(\mathrm{H})}$ (2)	$\log M_{\mathrm{ion}}^a$ $(M_\odot)$ (3)	$\dot{M}_{\mathrm{ion}}^a$ $(M_\odot\,\mathrm{yr}^{-1})$ (4)	$\log M_{\mathrm{ion}}^b$ $(M_\odot)$ (5)	$\dot{M}_{\mathrm{ion}}^b$ $(M_\odot\,\mathrm{yr}^{-1})$ (6)
NGC 5728	−5.1	4.0	0.08	3.8	0.04
NGC 5506	−5.2	4.3	0.28	4.1	0.12
ESO137-G034	−5.3	4.7	0.33	4.4	0.09
NGC 7172	−5.2	3.8	0.03	3.2	0.005
MCG-05-23-016	−5.3	4.0	0.04	3.3	0.004
NGC 3081	−4.9	4.0	0.03	3.2	0.007

Note. Column (1): galaxy name. Column (2): Ne^{4+} abundance relative to H ions (see Equation (B5)). Columns (3) and (4): ionized gas mass derived from the total [Ne V] flux and corresponding ionized gas outflow rates from the $r = 0\rlap{.}''9$ aperture. Columns (5) and (6): ionized gas mass derived from the flux of the broad component in [Ne V] emission line and corresponding ionized gas outflow rates from the $r = 0\rlap{.}''9$ aperture.

as the proxy of ionized gas mass in outflows. The [Ne V] emission line is used for the derivation as the kinematics of this high ionization potential line are dominated by outflows in the six targets. See Appendix B for the derivation of ionized gas mass, and see also Davies et al. (2020b) for the same strategy of calculating ionized gas mass in outflows but based on the [O III] 5007 Å emission. Following previous studies (e.g., Kakkad et al. 2022; Riffel et al. 2023), we take $\dot{M}_{\mathrm{ion}} = M_{\mathrm{ion}} W_{80}/R$, where M_{ion}, W_{80}, and R are, respectively, the ionized gas mass derived from the total [Ne V] flux, the flux-weighted W_{80} of [Ne V] emission line, and the flux-weighted distance to the AGN of spaxels within the circular aperture.

Meanwhile, we estimate for each target a rough lower limit of the integrated ionized gas outflow rate from the same $r = 0\rlap{.}''9$ aperture. These lower limits take the ionized gas mass derived from the flux of the broad component in [Ne V] emission line of all spaxels within the circular aperture as the proxy of ionized gas mass in outflows. In accordance with previous studies (e.g., Rupke et al. 2005; Fiore et al. 2017; Fluetsch et al. 2019; Venturi et al. 2023), we take $\dot{M}_{\mathrm{ion}} = M_{\mathrm{ion}} v_{\mathrm{out}}/R$ with $v_{\mathrm{out}} = v_{\mathrm{comp.\,2}} + 1.18\sigma_{\mathrm{comp.\,2}}$, where the comp.2 indicates the measurement of the broad component (see Appendix A). M_{ion}, v_{out}, and R are, respectively, the ionized gas mass derived from the flux of the broad component in [Ne V] emission line, the flux-weighted v_{out} of the broad component in [Ne V] emission line, and the flux-weighted distance to the AGN of spaxels within the circular aperture. See Table 4 for the calculated outflow rates of the six targets.

As shown in Figure 18, for most of the targets, the outflow rates calculated based on the total [Ne V] flux are consistent with those calculated by Davies et al. (2020b) based on the total [O III] flux, with the discrepancy within their quoted uncertainty (i.e., 0.21 dex). However, for NGC 7172 and MCG-05-23-016, the outflow rates calculated based on the total [Ne V] emission are larger by about an order of magnitude, plausibly due to the factor of dust obscuration (see Hermosa Muñoz et al. 2024a for more detailed discussion). The optical [O III] 5007 Å emission line is much more susceptible to dust extinction, whereas the correction of the [Ne V] flux for the six targets is less than 15% with the estimated dust extinction based on the extinction curve measured by García-Bernete et al. (2024a) combining the measured and theoretical Pfα/Huα ratios.

Figure 18 also shows that the outflow rates reported here are consistent with the best-fit correlation between the ionized gas
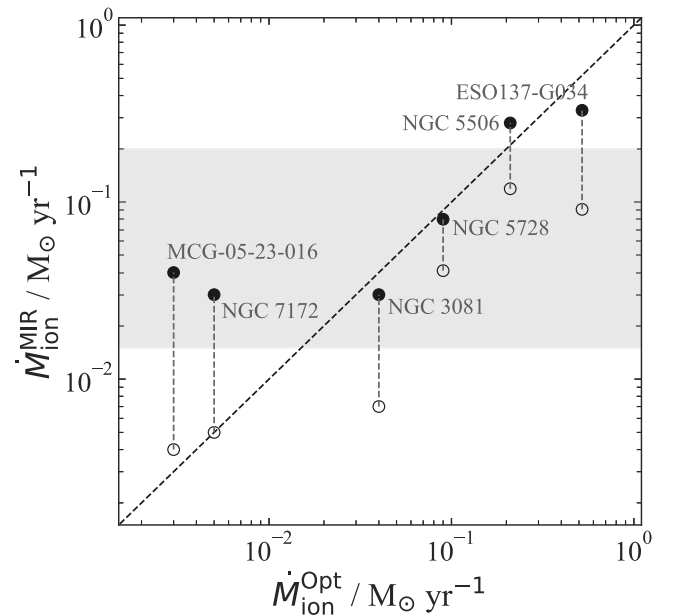
Figure 18. Comparison between ionized gas outflow rates derived from the [Ne V] 14.322 μm emission line as the y-axis and those from the optical [O III] 5007 Å emission line as the x-axis. The filled and blank circles correspond to outflow rates calculated based on the total [Ne V] emission and the broad component in [Ne V] emission, respectively. The gray shadowed region represents the range of ionized gas outflow rates (i.e., ~0.015–0.2 $M_\odot\,\mathrm{yr}^{-1}$) according to the best-fit correlation in Figure 1 of Fiore et al. (2017), given the AGN luminosity of the six targets (i.e., ~$10^{43.4}$–$10^{44.3}$ erg s^{-1}).

outflow rate and the AGN luminosity obtained by Fiore et al. (2017) for AGN with relatively higher luminosity (i.e., $L_{\mathrm{bol}} \approx 10^{44.5}$–$10^{48.0}$ erg s^{-1}). This result verifies the outflow rates reported here are physically reliable. More importantly, averaging the measurements as shown in Figure 18 for reference, the ionized outflow rates of the six targets are converged to a narrower range than the previous finding (i.e., Davies et al. 2020b). This result indicates the measurement accuracy, especially that of the outflowing ionized gas mass, could be one reason for the observed diversity of ionized outflow rates for AGN with the comparable luminosity. Accordingly, to fully understand the diversity of outflow strength in AGN of the comparable luminosity, a more dedicated study of a large sample with an accurate outflow rate measurement is indispensable.

6. Summary and Conclusions

This paper leverages the JWST MIRI/MRS IFU observations to display the diversity of ionized gas distributions and kinematics in central kiloparsec-scale regions of six nearby Seyfert galaxies (Section 2). Specifically, we explore the spatially resolved flux distributions and velocity fields of six ionized emission lines covering a large range of ionization potentials (Sections 3.2.1 and 3.2.2).

We find the evidence of ionized gas outflows in the six targets, according to the twisting between velocity fields of six emission lines (for NGC 5728, NGC 5506, NGC 3081, and likely ESO137-G034), and combining the observed ionized line ratios with theoretical calculations (for NGC 7172, and MCG-05-23-016). Meanwhile, we find NGC 5728, NGC 5506, and ESO137-G034 also exhibit some intriguing highly disturbed regions (Section 3.2.3). For these three targets, their integrated spectra also exhibit broader ionized emission lines than the others (Section 3.1).

We further discuss case by case the possible triggering mechanisms of such highly disturbed regions in these three targets (Section 4). We propose that the radio jet associated with AGN activity plausibly plays an important role in triggering such highly disturbed regions. Accordingly, we provide a phenomenological model involving radio jets to illustrate the potential outflow structures of the three targets. To further this work, detailed analysis and modeling of the physical conditions in these regions are required.

Moreover, we have a rather quantitative comparison of the outflow strength among the six targets (Section 5). With the outflow rates calculated based on [Ne V] emission, which is relatively immune to dust obscuration, we find the six targets tend to have the ionized outflow rates converged to a narrower range than the previous finding. These results have an important implication for the diverse outflow properties of AGN with the comparable luminosity, while more convincing conclusions require further dedicated analysis.

Acknowledgments

Appendix A
Characteristics of Outflows with Parametric Measurements

The parametric method is widely used to study AGN-driven outflows, although caveats are required when used in this work (Section 2.4). As a supplementary analysis, here, we briefly discuss the flux distribution ($f_{\rm comp.\,2}$), the velocity field ($v_{\rm comp.\,2}$), and the velocity dispersion field ($\sigma_{\rm comp.\,2}$), of the relatively broader component, if included (see Section 2.3), in the best-fit [Ne II] and [Ne V] profiles. For NGC 5728, NGC 5506, ESO137-G034, and NGC 3081, their $f_{\rm comp.\,2}$ distributions of [Ne II] and [Ne V] emission lines are similar to each other, and the same for the $v_{\rm comp.\,2}$ fields. Moreover, for both [Ne II] and [Ne V] emission lines, their $f_{\rm comp.\,2}$ and $v_{\rm comp.\,2}$ distributions are respectively similar to $f_{\rm total}$ and v_m distributions of the [Ne V] emission line. This result supports that $f_{\rm total}$ and v_m distributions of the [Ne V] emission line mainly trace ionized gas outflow features. The above result is not that evident for the other two targets. We also note that $v_{\rm comp.\,2}$ distributions of ESO137-G034 are more disturbed around the two KDRs. This result cautions against the use of parametric methodology for systems with complex outflow features. Additionally, for NGC 5728, NGC 5506, and ESO137-G034, their $\sigma_{\rm comp.\,2}$ distributions of the [Ne V] emission line also exhibit some highly disturbed regions (i.e., regions with very large $\sigma_{\rm comp.\,2}$) that are perpendicular to their AGN ionization cones. This result confirms similar findings as revealed by their W_{80} distributions in Section 3.2.3.

Appendix B
Derivation of Ionized Gas Mass

To calculate the ionized gas outflow rate, we need to first derive the ionized gas mass from the observed strength of ionized gas emission. This section uses the [Ne V] 14.322 μm emission line as an example for the derivation, as it is most sensitive to the AGN ionization among the six lines and most likely traces ionized gas outflows.

In theory, the [Ne V] luminosity can be derived by

$$L_{\text{[Ne V]}} = \int_V f n_e \, n(\text{Ne}^{4+}) j_{\text{[Ne V]}}(n_e, T_e) dV, \qquad (B1)$$

where f, n_e, $n(\text{Ne}^{4+})$, and $j_{\text{[Ne V]}}(n_e, T_e)$ are the filling factor, the electron density, the Ne^{4+} density, and the [Ne V] emissivity at given electron density and electron temperature, respectively (Draine 2011). Therein, $n(\text{Ne}^{4+})$ can be obtained as $n(\text{Ne}^{4+}) = \frac{n(\text{Ne}^{4+})}{n(\text{H})} \frac{n(\text{H})}{n_e} n_e$, with $\frac{n(\text{H})}{n_e} \approx \frac{n(\text{H})}{n(\text{H}) + 2 \times n(\text{He})} = (1.2)^{-1}$ assuming $\frac{n(\text{He})}{n(\text{H})} = 0.1$. Accordingly, the [Ne V] luminosity is derived as

$$L_{\text{[Ne V]}} = (1.2)^{-1} f \frac{n(\text{Ne}^{4+})}{n(\text{H})} j_{\text{[Ne V]}}(n_e, T_e) \langle n_e^2 \rangle V, \qquad (B2)$$

where $\langle n_e^2 \rangle$ is the volume-averaged squared electron density.

Meanwhile, the ionized gas mass can be derived by

$$M_{\text{ion}} \simeq \int_V f n(\text{H}) \overline{m} dV, \qquad (B3)$$

where $\overline{m}$ is the average molecular-weighted mass. Specifically, we adopt $n(\text{H})\overline{m} \approx n_e \frac{n(\text{H})}{n_e} \frac{n(\text{H})m_p + 4 \times n(\text{He})m_p}{n(\text{H}) + n(\text{He})} \approx n_e (1.2)^{-1} 1.2 m_p = n_e m_p$ (Carniani et al. 2015), where m_p is the proton mass, again assuming $\frac{n(\text{He})}{n(\text{H})} = 0.1$. Accordingly, the ionized gas mass is derived as

$$M_{\text{ion}} \simeq f \langle n_e \rangle m_p V, \qquad (B4)$$

where $\langle n_e \rangle$ is the volume-averaged electron density.

Combining Equations (B2) and (B4), the ionized gas mass is finally derived as

$$M_{\text{ion}} = \frac{1.2 \frac{\langle n_e \rangle^2}{\langle n_e^2 \rangle} L_{\text{[Ne V]}} m_p}{\frac{n(\text{Ne}^{4+})}{n(\text{H})} \langle n_e \rangle j_{\text{[Ne V]}}(n_e, T_e)}, \qquad (B5)$$

where we adopt $\frac{\langle n_e \rangle^2}{\langle n_e^2 \rangle} = 1$ and $\frac{n(\text{Ne}^{4+})}{n(\text{H})} = \frac{I_{\text{[Ne V]}}}{j_{\text{[Ne V]}}} / \frac{I_{\text{Pf}\alpha}}{j_{\text{Pf}\alpha}}$, and I_{line} and j_{line} denote line intensity and line emissivity, respectively. Pfα emission line is used here as it is the strongest hydrogen recombination line covered by our MRS spectral observations and can be replaced by other hydrogen recombination lines if available.

Since the relatively weak Pfα emission is not available for all spatially resolved spaxels, an unresolved $\frac{n(\text{Ne}^{4+})}{n(\text{H})}$ value (see Table 4) is calculated for each target based on the aperture measurements as listed in Table 3. The line emissivity $j_{\text{line}}(n_e, T_e)$ is obtained by PyNeb, a modern Python tool to compute emission line emissivities (Luridiana et al. 2015). Emissivities of these emission lines have very weak dependence on T_e for high temperature environments, and hence, we assume a standard value of $T_e = 10^4$ K (Fernández-Ontiveros et al. 2021; Pérez-Díaz et al. 2022). $\langle n_e \rangle$ is obtained as $n_e = 3.2 (\frac{L_{\text{bol}}}{10^{45} \, \text{erg s}^{-1}}) (\frac{r}{1 \, \text{kpc}})^{-2} \frac{1}{U}$ cm^{-3} according to Baron & Netzer (2019), and see Table B1 for the radial n_e profile of each target. Specifically, the ionization parameter U can be derived from measured [S IV]/[Ne III] line ratios (i.e., Pereira-Santaella et al. 2017).

According to the emission line ratio diagram (i.e., [Ne V]/[Ne II] versus [Ne III]/[Ne II]) with model results calculated by Morisset et al. (2015) and Pereira-Santaella et al. (2024), the central regions of the six targets are dominated by AGN excitation or fast radiative shocks associated with the AGN. Therefore, we calculate the U based on the correlation between U and [S IV]/[Ne III] of AGN models in Pereira-Santaella et al. (2017), assuming the solar metallicity and $n_H = 10^3$ cm^{-3}. The log U distributions of the six targets are found to have the median values of ~ -2.9 to -2.6, with the standard deviations of ~ 0.1–0.3 dex within their field of view. These results are consistent with the values derived by Davies et al. (2020b) in an independent way for these targets. This supports the assumptions we adopted here for calculating the ionization parameter. Around the median values of ~ -2.9 to -2.6, the derived U value varies within ~ 0.3 dex for $Z = 0.04$–$2 \, Z_\odot$ and $n_H = 10$–10^4 cm^{-3} (see Figure B2 in Pereira-Santaella et al. 2017). Note that the calculation of n_e based on the ionization parameter U is only for the rather quantitative comparison in Section 5. Specific work in terms of the n_e derivation based on emission line pairs (e.g., [Ne V] 14.32 & 24.32 μm, [Ar V] 7.90 & 13.10 μm) covered by JWST spectra is in preparation.

Table B1
The Radial Profile of n_e Distribution

NGC 5728		NGC 5506		ESO137-G034		NGC 7172		MCG-05-23-016		NGC 3081	
r (pc)	log n_e (cm^{-3})	r (pc)	log n_e (cm^{-3})	r (pc)	log n_e (cm^{-3})	r (pc)	log n_e (cm^{-3})	r (pc)	log n_e (cm^{-3})	r (pc)	log n_e (cm^{-3})
(1)	(2)	(3)	(4)	(5)	(6)	(7)	(8)	(9)	(10)	(11)	(12)
59	5.0	44	5.2	57	4.2	58	5.0	57	5.3	56	4.8
156	4.0	105	4.4	136	3.3	145	4.2	148	4.4	135	4.0
280	3.5	200	3.9	255	2.9	269	3.6	258	3.9	246	3.5
410	3.2	288	3.6	370	2.7	394	3.3	371	3.6	358	3.2
539	3.0	375	3.3	486	2.4	514	3.0	484	3.3	468	3.0
667	2.9	463	3.1	597	2.2	632	2.8	599	3.0	581	2.7

Note. Column (1): radius r, for the first row is the median radius of the innermost five spaxels, and for other rows is the median radius for spaxels in a 0″7 width annulus used to calculate the median electron density. Column (2): log n_e, for the first row is the median electron density of the innermost five spaxels, and for other rows is the median electron density for spaxels in a 0″7 width annulus.

Appendix C
Atlas of Emission Line Flux Distributions and Velocity Fields

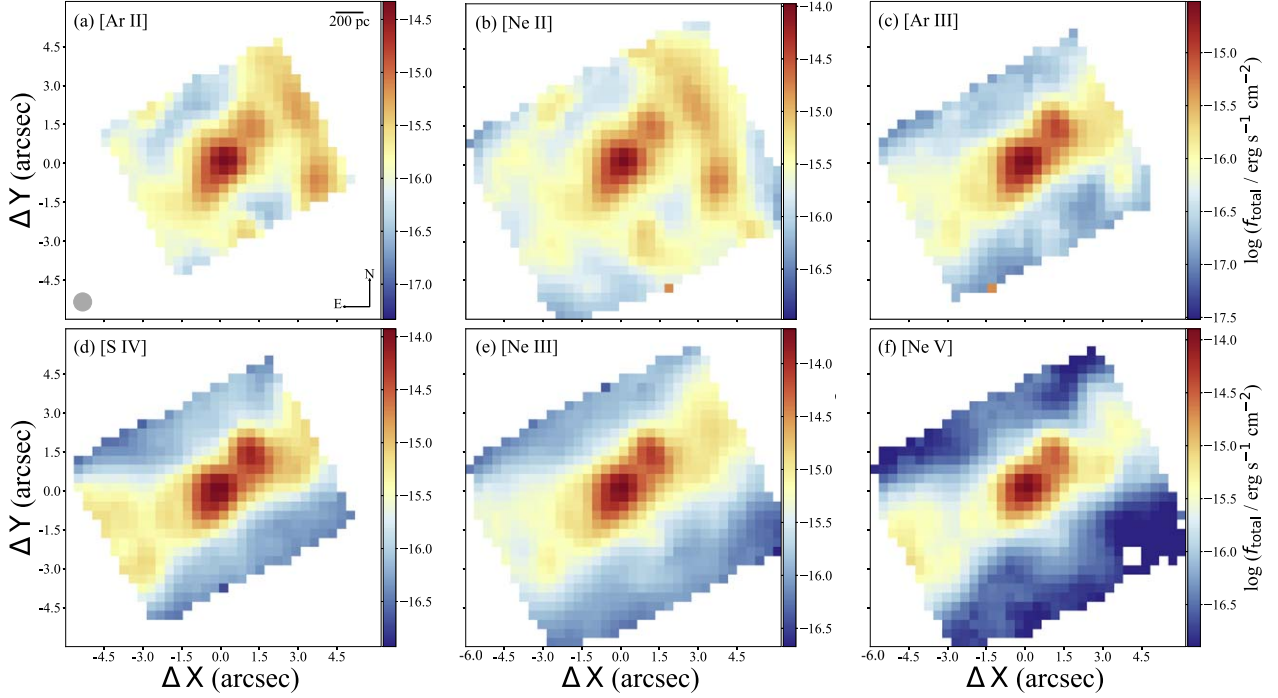Figures C1–C18 show spatially resolved maps of six emission lines for the six targets.
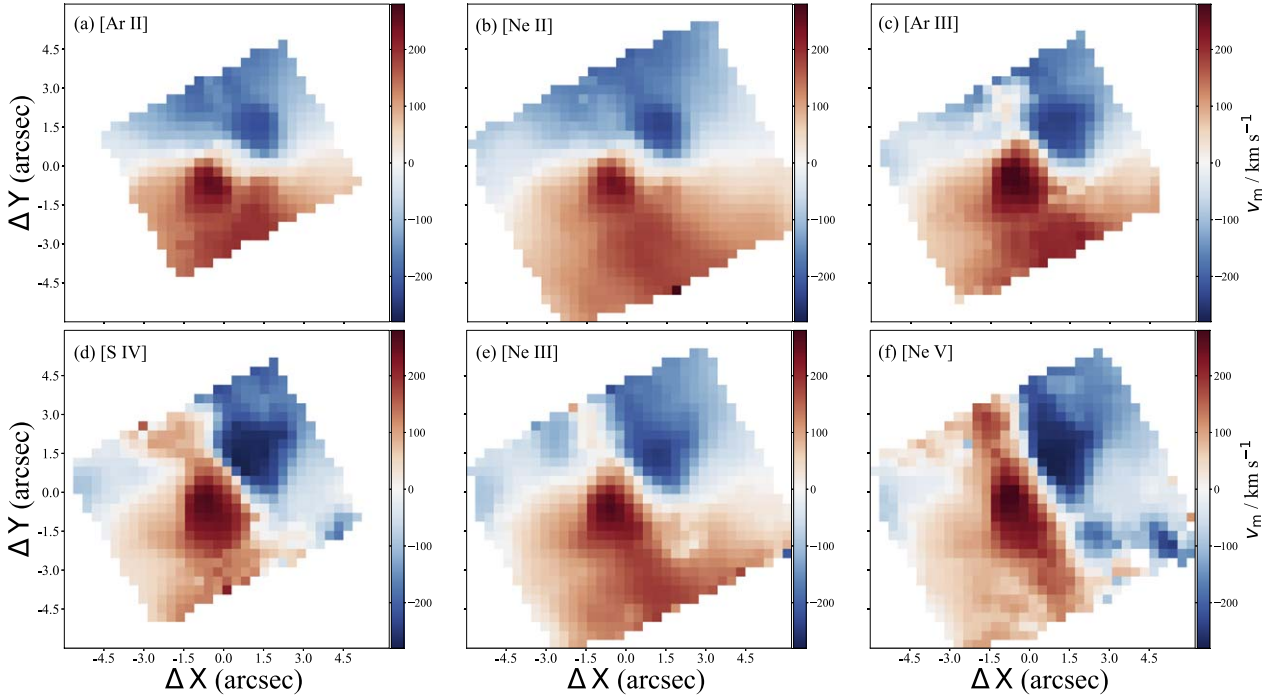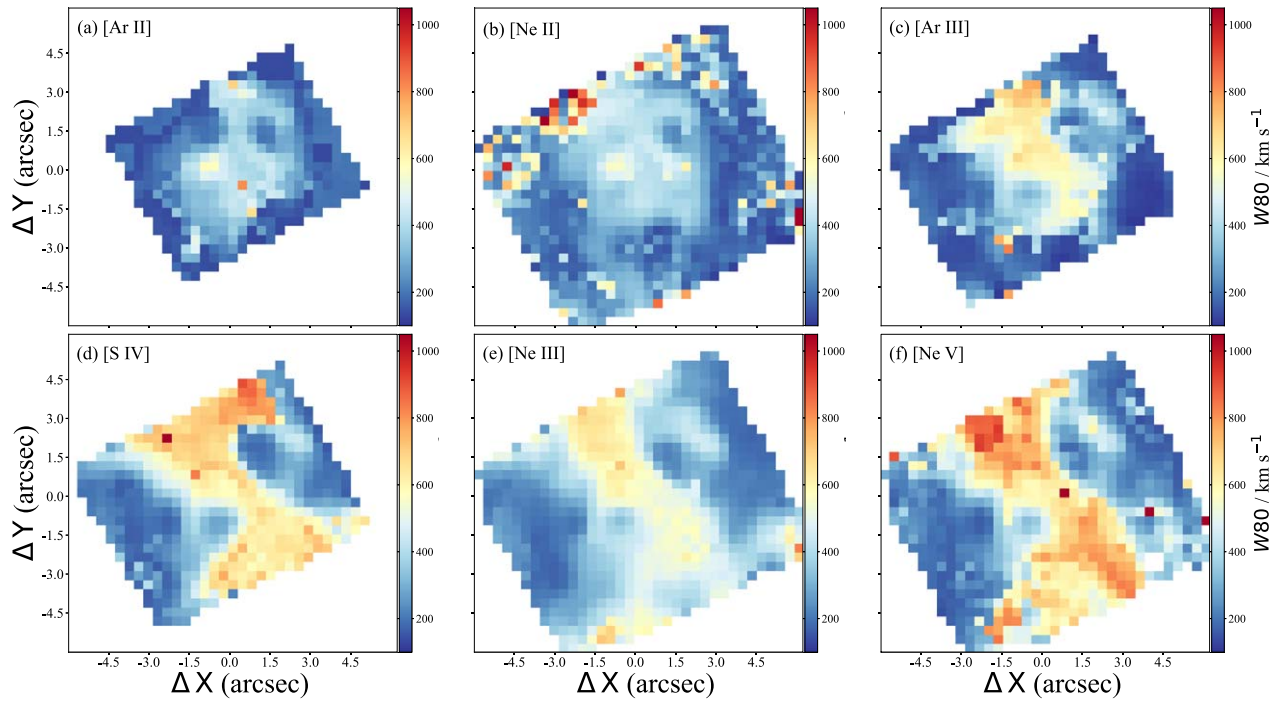

Figure C1. The f_{total} distributions in NGC 5728 central region for emission lines of (a) [Ar II] 6.985 μm with the ionization potential (IP) of 15.8 eV, (b) [Ne II] 12.814 μm with the IP of 21.6 eV, (c) [Ar III] 8.991 μm with the IP of 27.6 eV, (d) [S IV] 10.511 μm with the IP of 34.8 eV, (e) [Ne III] 15.555 μm with the IP of 41.0 eV, and (f) [Ne V] 14.322 μm with the IP of 97.1 eV. Panel (a) features a filled gray circle to indicate the angular resolution of these maps (i.e., $0\farcs7 \times 0\farcs7$), a compass (with N is up, and E is to the left), and a scale bar of 200 pc; they are the same for all panels here, and for all subsequent maps belonging to NGC 5728.

Figure C2. The v_m distributions in NGC 5728 central region for emission lines of (a) [Ar II] 6.985 μm with the ionization potential (IP) of 15.8 eV, (b) [Ne II] 12.814 μm with the IP of 21.6 eV, (c) [Ar III] 8.991 μm with the IP of 27.6 eV, (d) [S IV] 10.511 μm with the IP of 34.8 eV, (e) [Ne III] 15.555 μm with the IP of 41.0 eV, and (f) [Ne V] 14.322 μm with the IP of 97.1 eV.

Figure C3. The W_{80} distributions in NGC 5728 central region for emission lines of (a) [Ar II] 6.985 μm with the ionization potential (IP) of 15.8 eV, (b) [Ne II] 12.814 μm with the IP of 21.6 eV, (c) [Ar III] 8.991 μm with the IP of 27.6 eV, (d) [S IV] 10.511 μm with the IP of 34.8 eV, (e) [Ne III] 15.555 μm with the IP of 41.0 eV, and (f) [Ne V] 14.322 μm with the IP of 97.1 eV.
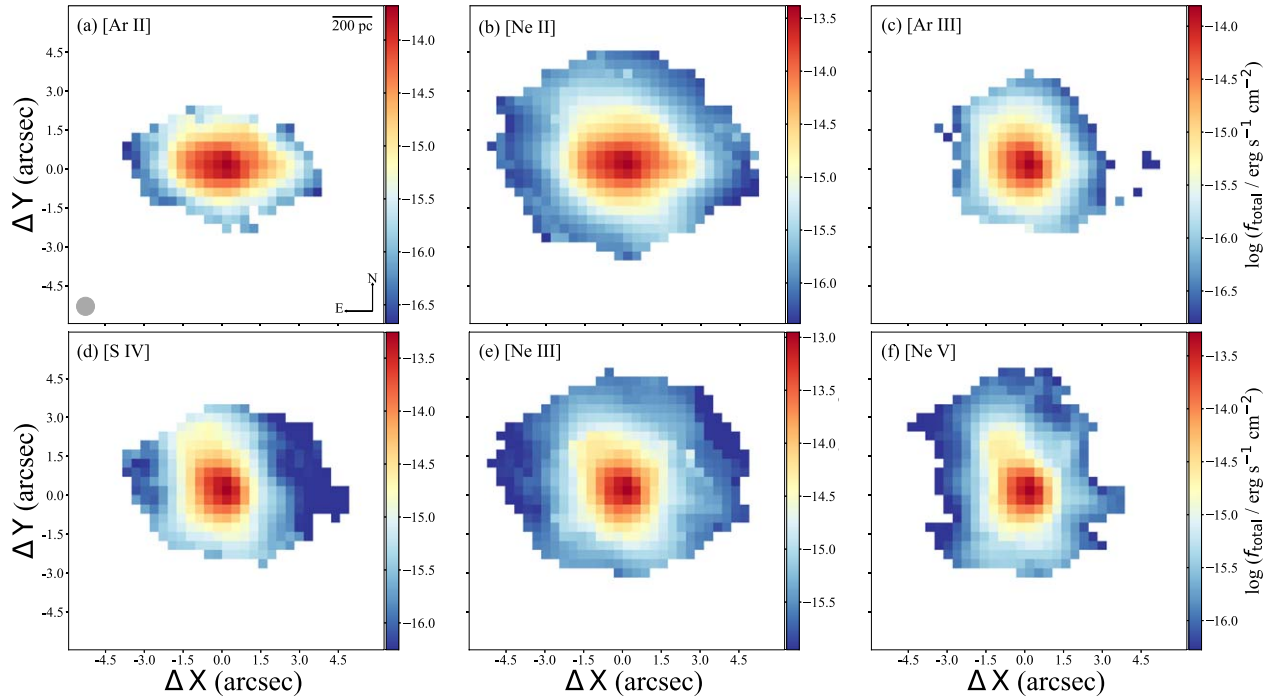
Figure C4. The same as Figure C1 but for NGC 5506.
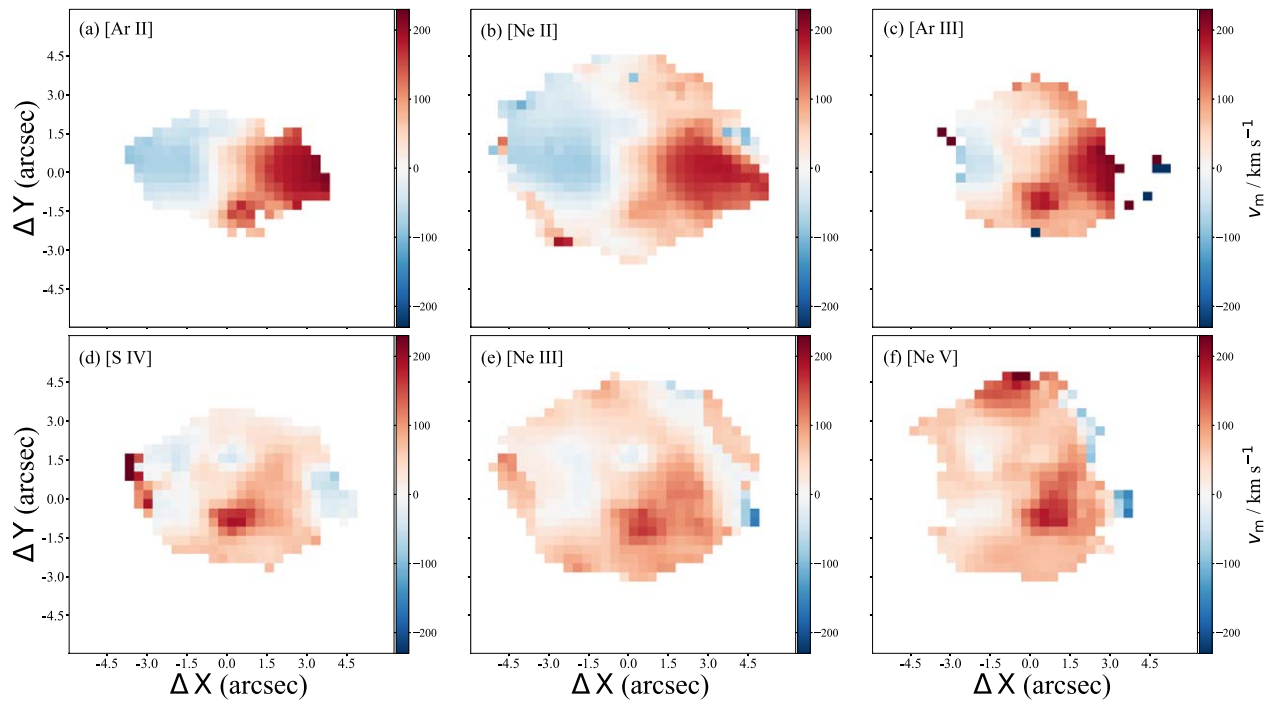
Figure C5. The same as Figure C2 but for NGC 5506.
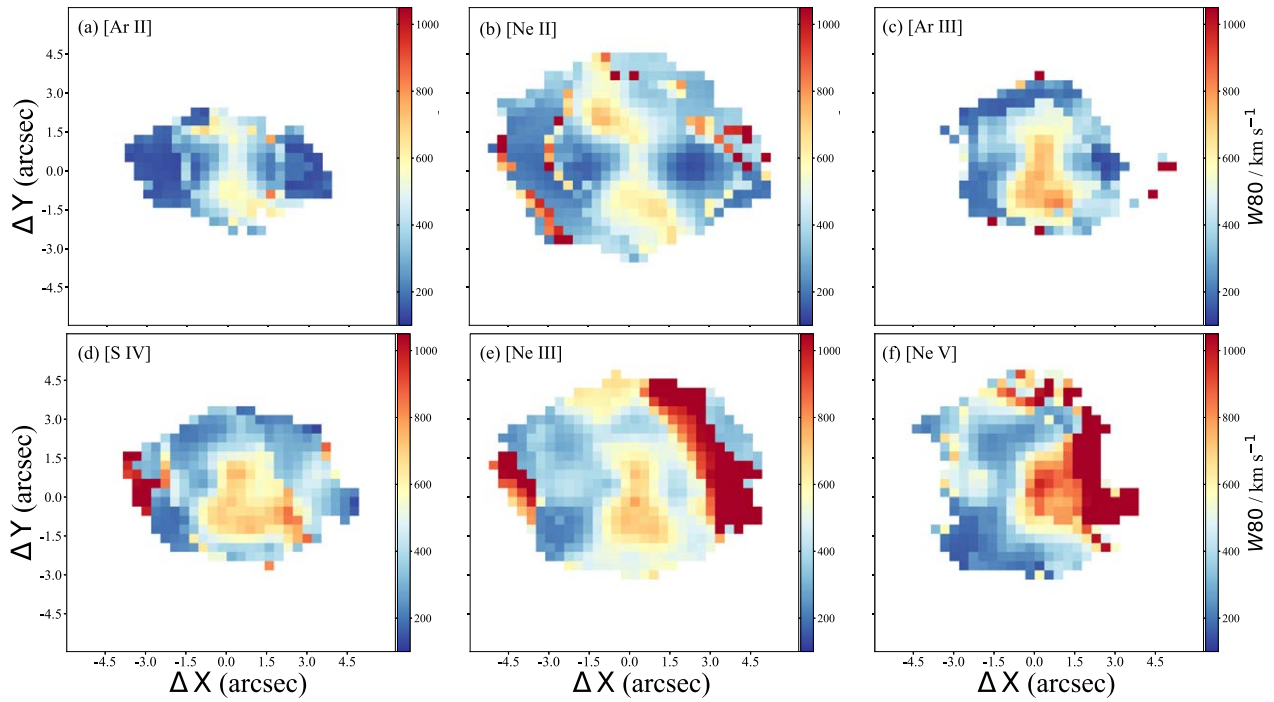
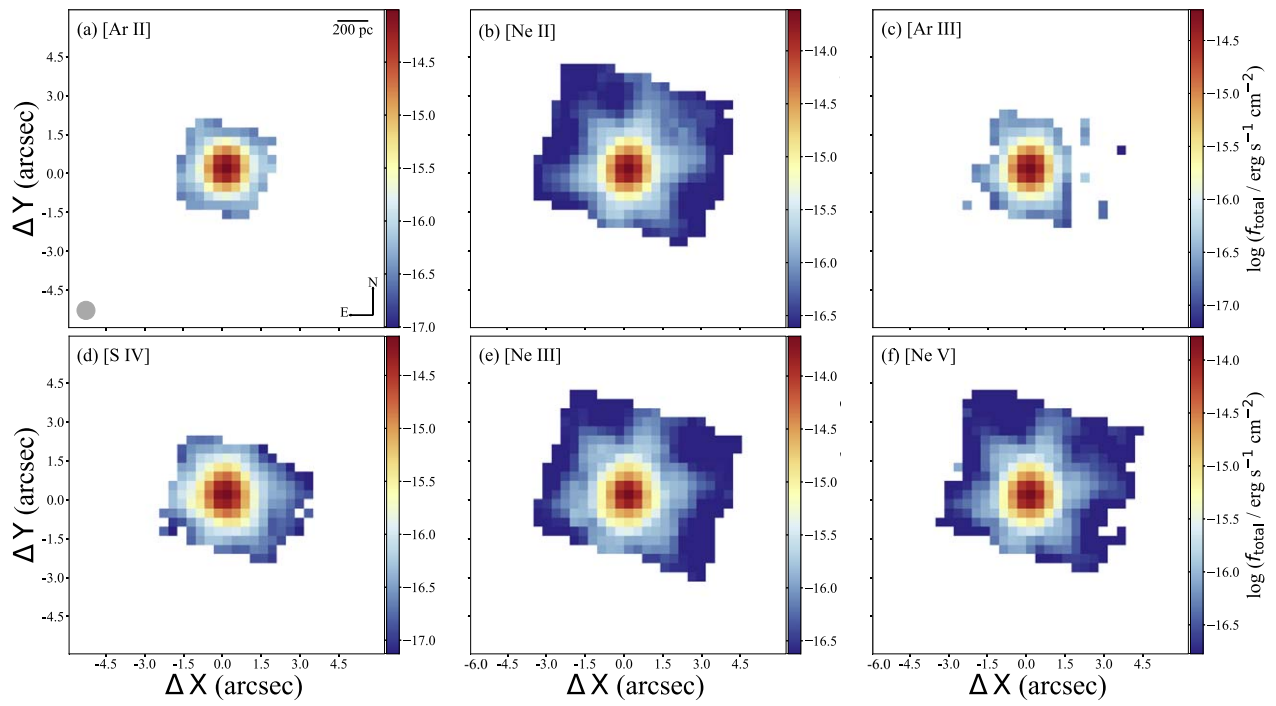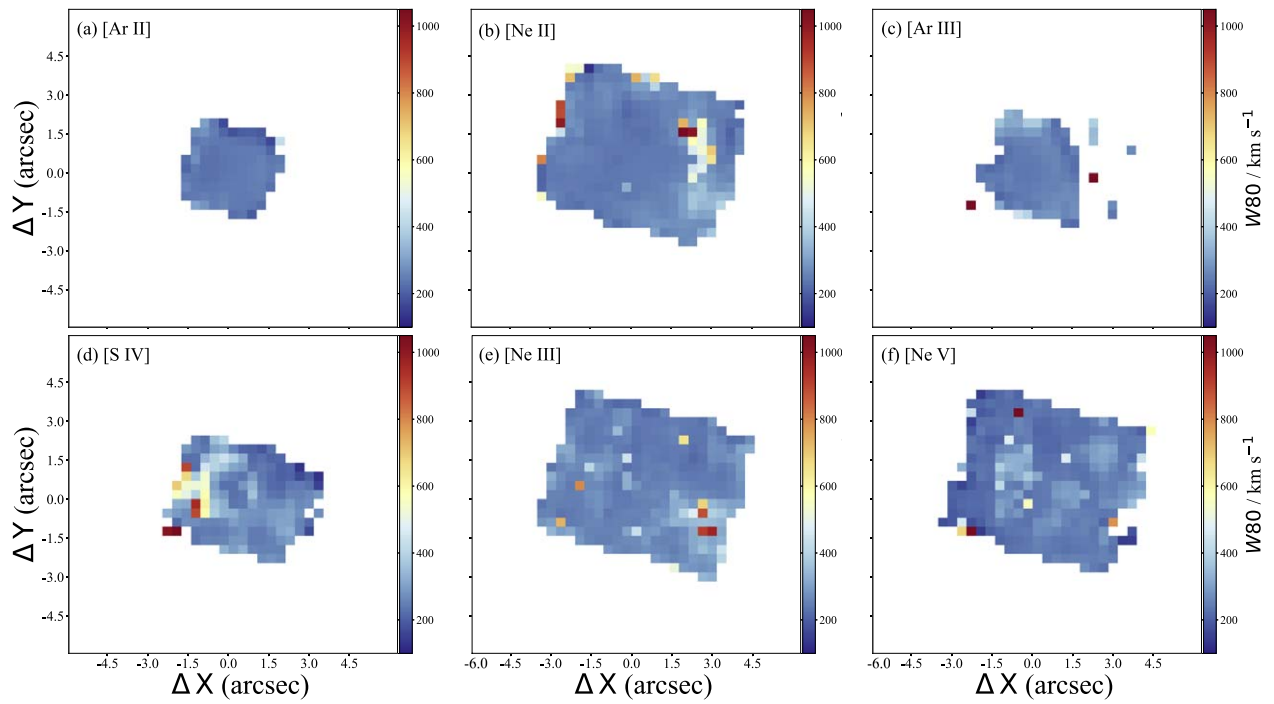

Figure C6. The same as Figure C3 but for NGC 5506.
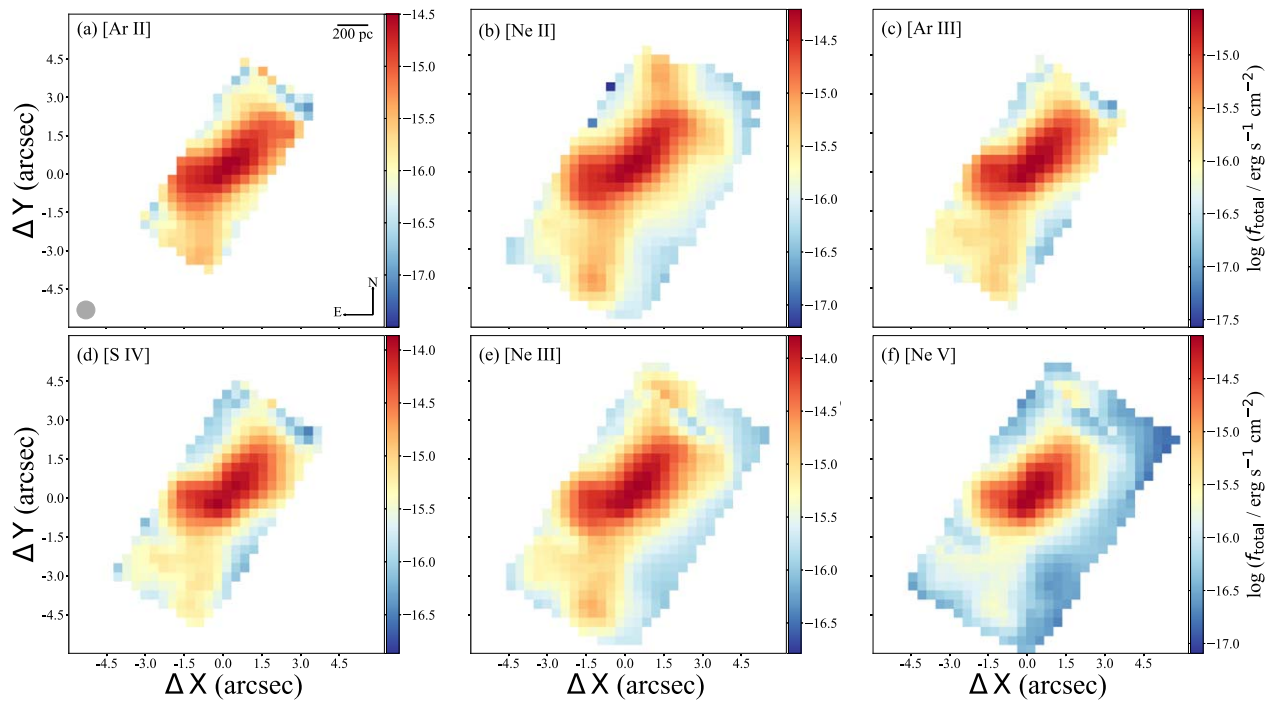
Figure C7. The same as Figure C1 but for ESO137-G034.
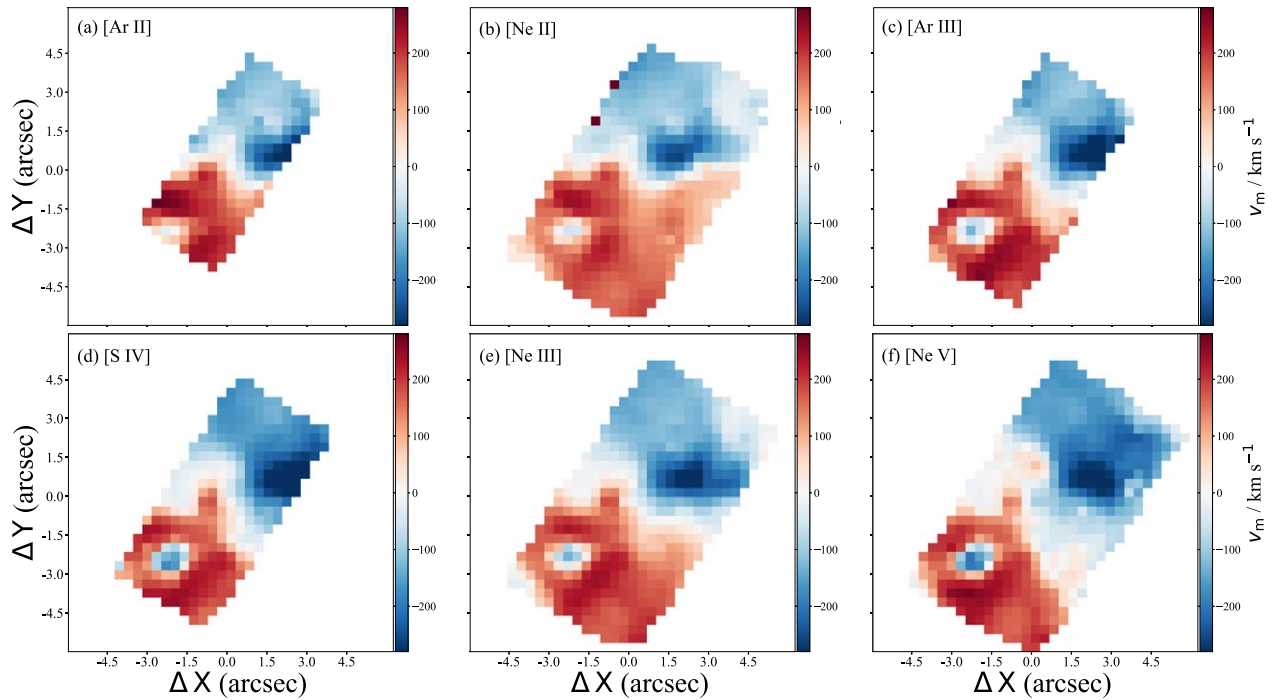
Figure C8. The same as Figure C2 but for ESO137-G034.
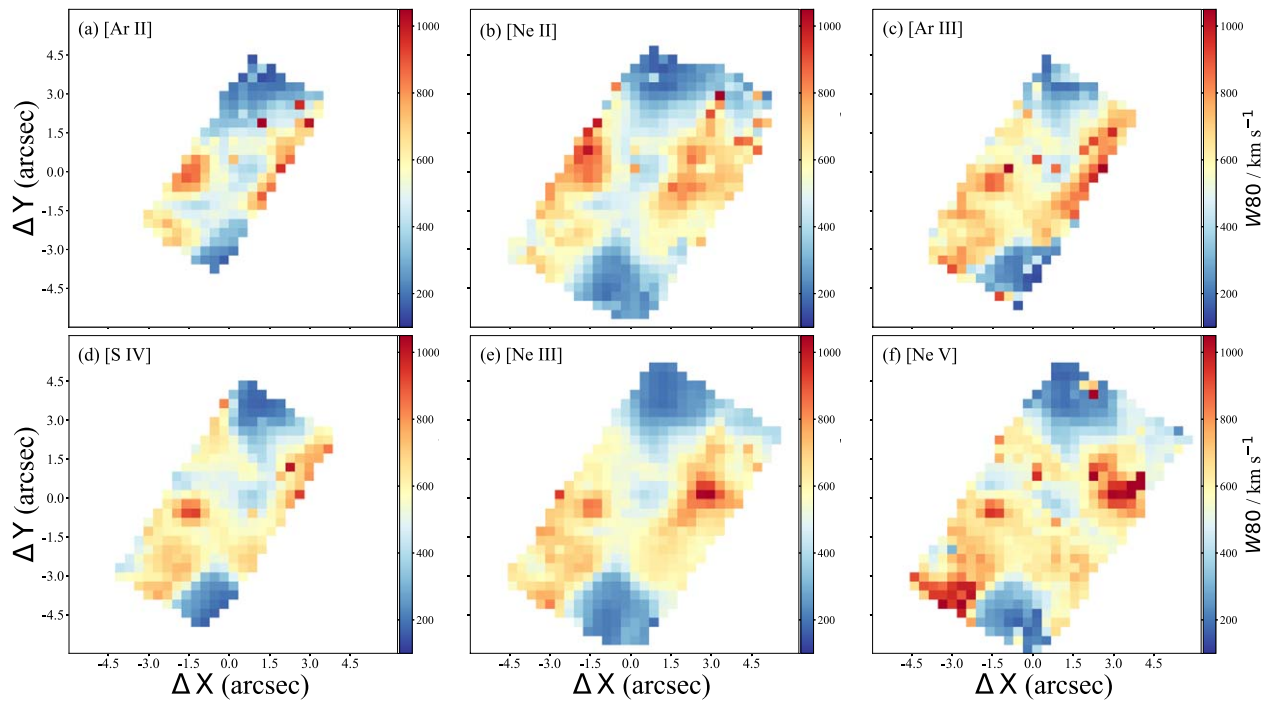
Figure C9. The same as Figure C3 but for ESO137-G034.
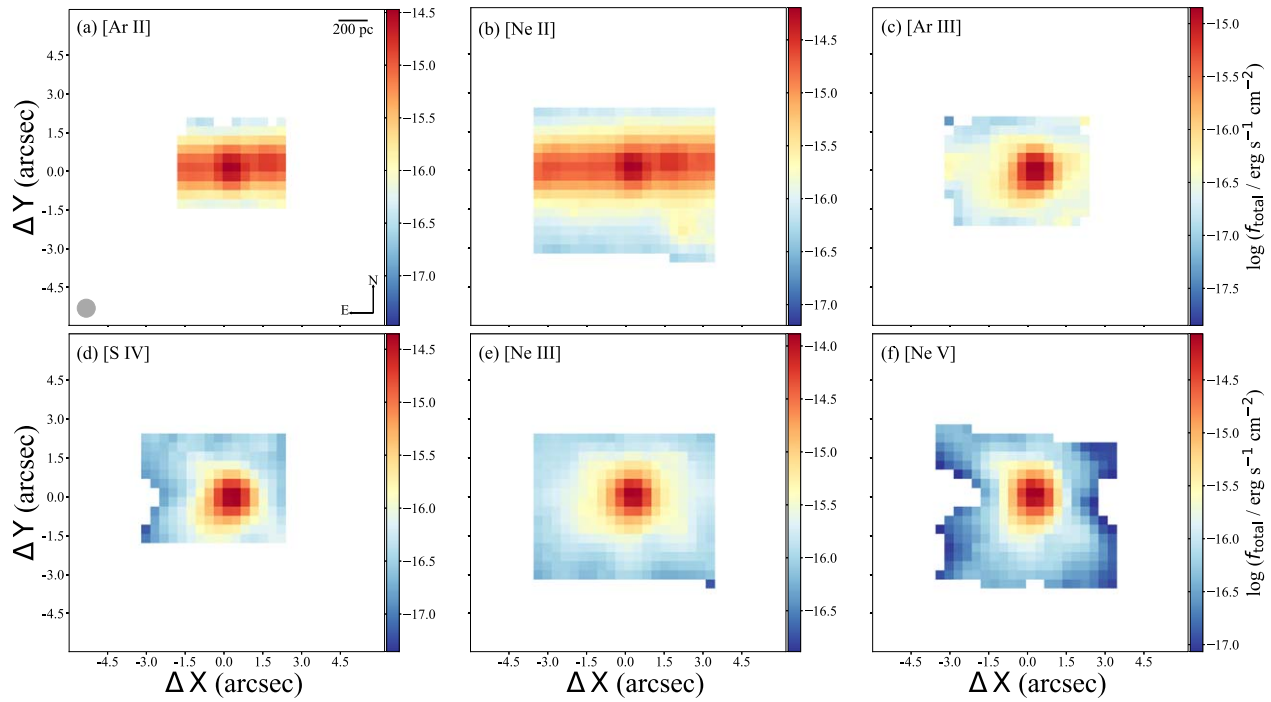
Figure C10. The same as Figure C1 but for NGC 7172.
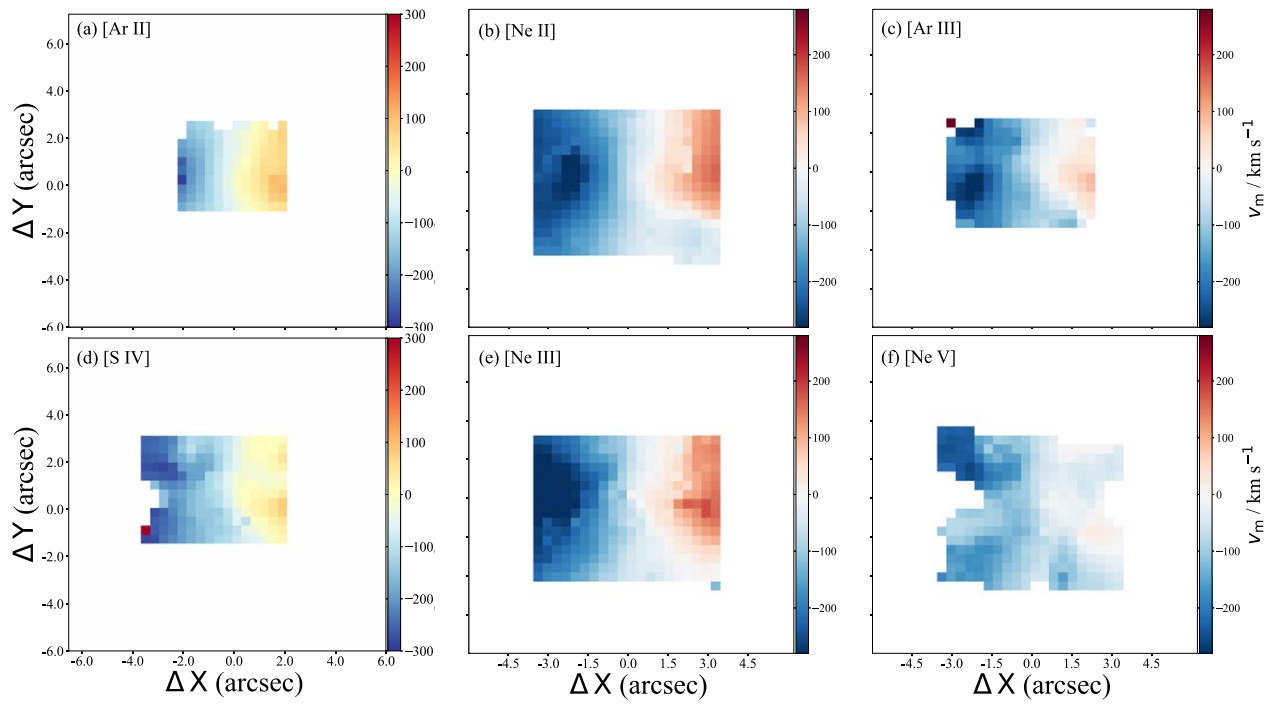
Figure C11. The same as Figure C2 but for NGC 7172.
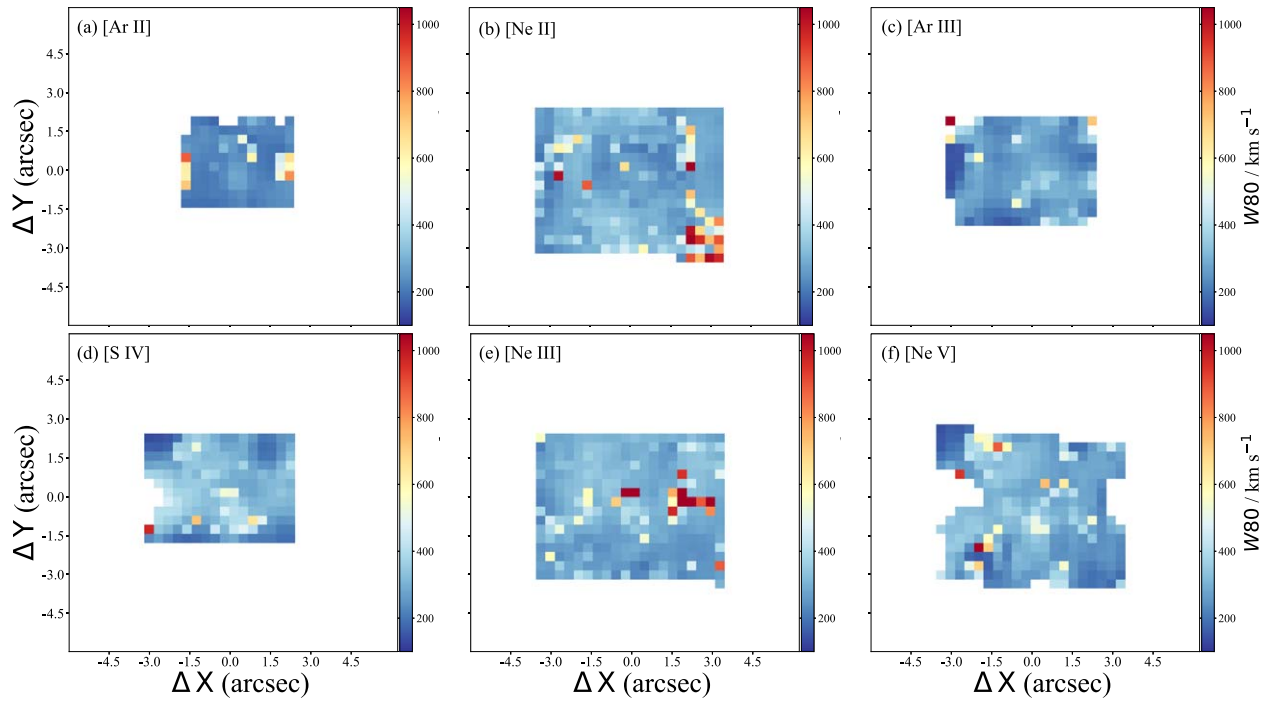
Figure C12. The same as Figure C3 but for NGC 7172.

Figure C13. The same as Figure C1 but for MCG-05-23-016.
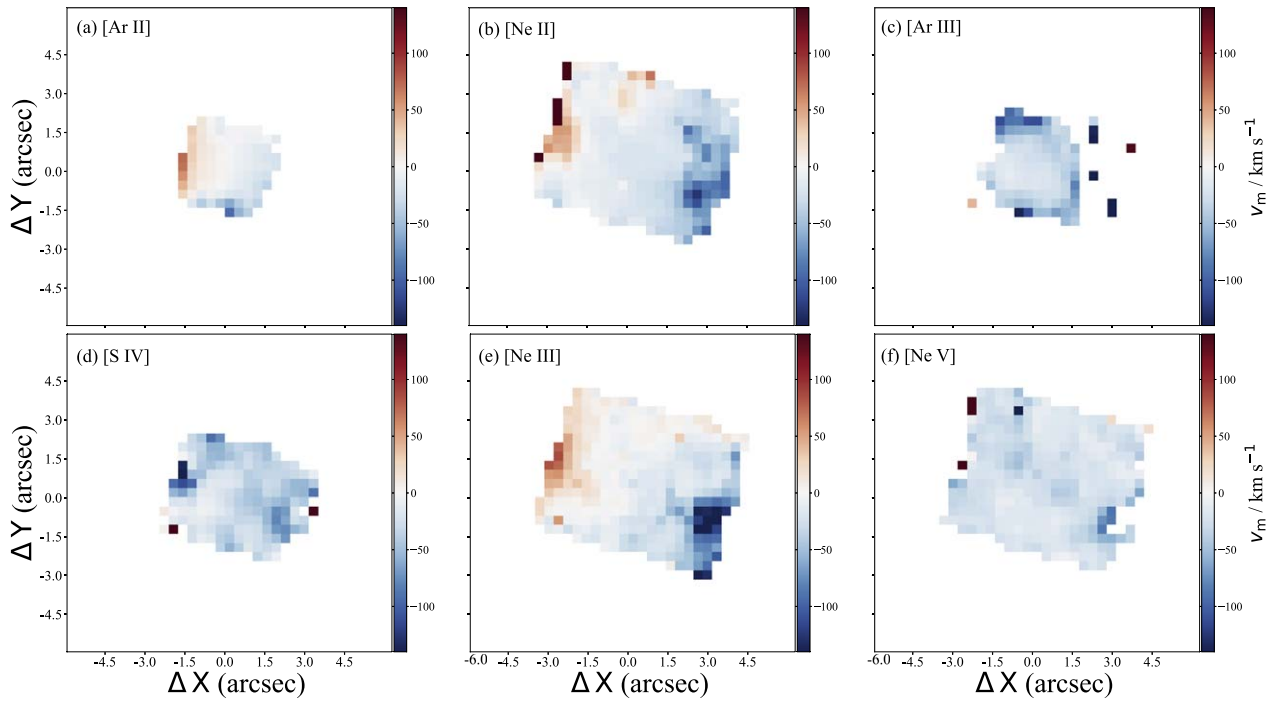
Figure C14. The same as Figure C2 but for MCG-05-23-016.

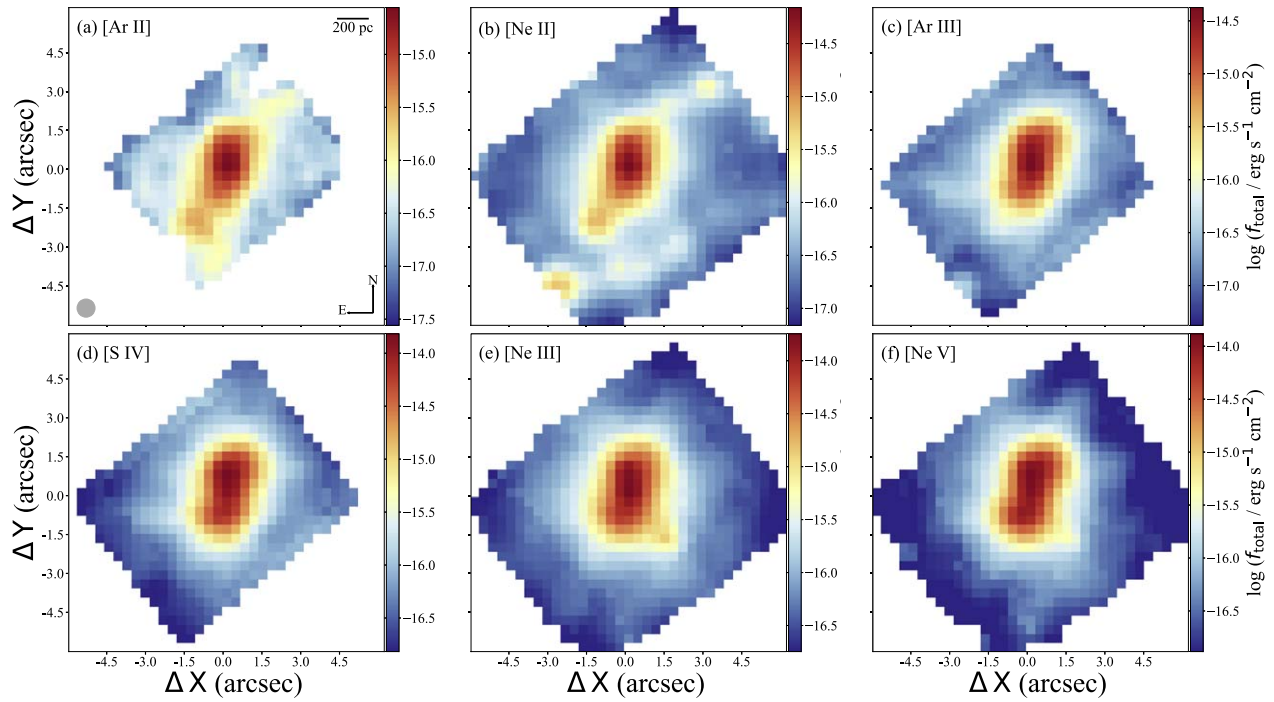**Figure C15.** The same as Figure C3 but for MCG-05-23-016.

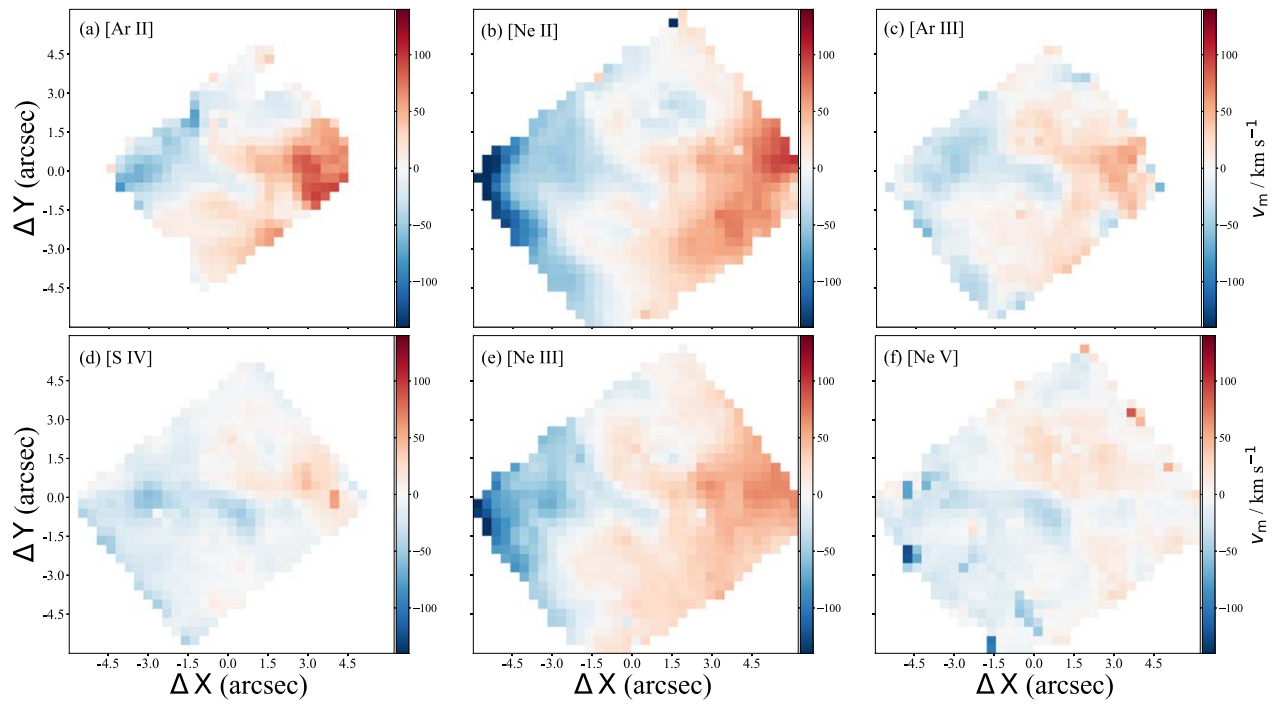**Figure C16.** The same as Figure C1 but for NGC 3081.
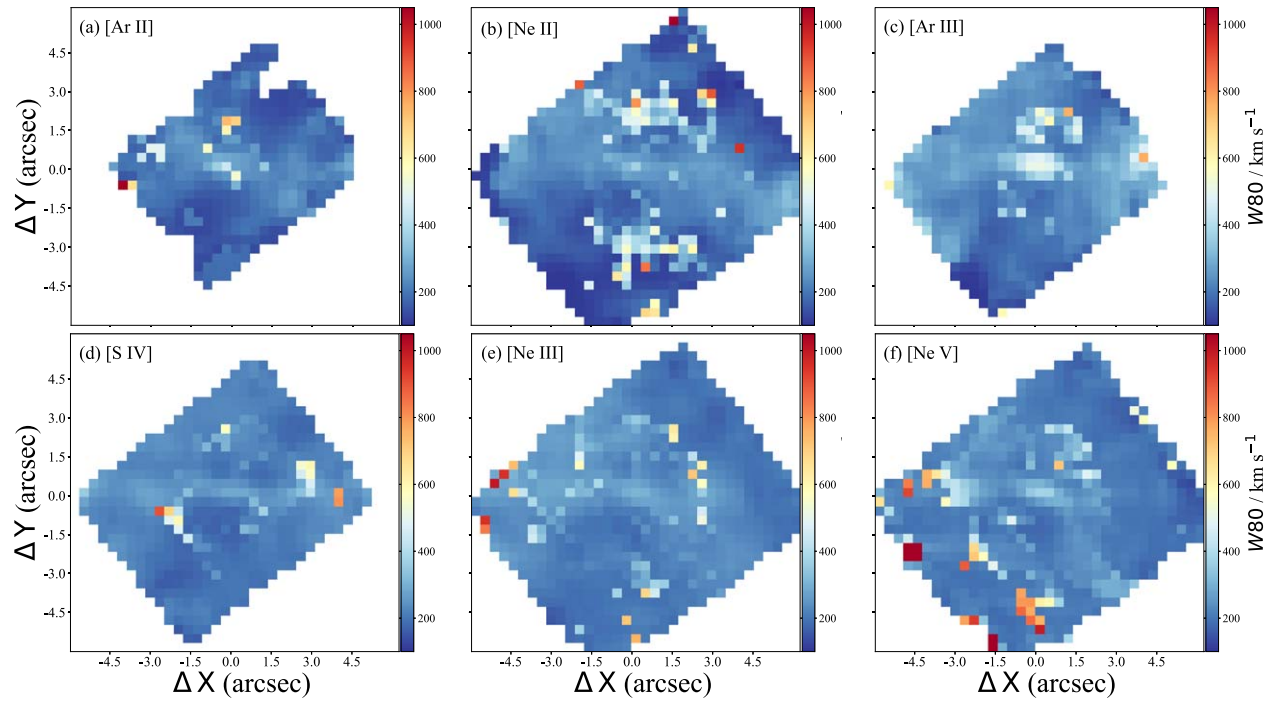
Figure C17. The same as Figure C2 but for NGC 3081.

Figure C18. The same as Figure C3 but for NGC 3081.

ORCID iDs

Lulu Zhang ⦿ https://orcid.org/0000-0003-4937-9077
Chris Packham ⦿ https://orcid.org/0000-0001-7827-5758
Erin K. S. Hicks ⦿ https://orcid.org/0000-0002-4457-5733
Taro T. Shimizu ⦿ https://orcid.org/0000-0002-2125-4670
Miguel Pereira-Santaella ⦿ https://orcid.org/0000-0002-4005-9619
Francoise Combes ⦿ https://orcid.org/0000-0003-2658-7893
Poshak Gandhi ⦿ https://orcid.org/0000-0003-3105-2615
Masatoshi Imanishi ⦿ https://orcid.org/0000-0001-6186-8792
Mason T. Leist ⦿ https://orcid.org/0000-0003-4975-2046
Nancy A. Levenson ⦿ https://orcid.org/0000-0003-4209-639X
Cristina Ramos Almeida ⦿ https://orcid.org/0000-0001-8353-649X
Claudio Ricci ⦿ https://orcid.org/0000-0001-5231-2645
Dimitra Rigopoulou ⦿ https://orcid.org/0000-0001-6854-7545
Marko Stalevski ⦿ https://orcid.org/0000-0001-5146-8330
Takuma Izumi ⦿ https://orcid.org/0000-0001-9452-0813

References

Alarie, A., & Morisset, C. 2019, RMxAA, 55, 377
Alonso-Herrero, A., García-Burillo, S., Hönig, S. F., et al. 2021, A&A, 652, A99
Alonso-Herrero, A., García-Burillo, S., Pereira-Santaella, M., et al. 2023, A&A, 675, A88
Aniano, G., Draine, B. T., Gordon, K. D., et al. 2011, PASP, 123, 1218
Argyriou, I., Glasse, A., Law, D. R., et al. 2023, A&A, 675, A111
Argyriou, I., Wells, M., Glasse, A., et al. 2020, A&A, 641, A150
Armus, L., Charmandaris, V., Bernard-Salas, J., et al. 2007, ApJ, 656, 148
Armus, L., Lai, T., U, V., et al. 2023, ApJL, 942, L37
Arribas, S., Colina, L., Bellocchi, E., et al. 2014, A&A, 568, A14
Asmus, D., Hönig, S. F., Gandhi, P., et al. 2014, MNRAS, 439, 1648
Audibert, A., Ramos Almeida, C., García-Burillo, S., et al. 2023, A&A, 671, L12
Bae, H.-J., & Woo, J.-H. 2016, ApJ, 828, 97
Barbary, K., Boone, K., Craig, M., et al. 2017, kbarbary/sep: v1.0.2, Zenodo, doi:10.5281/zenodo.896928
Baron, D., & Netzer, H. 2019, MNRAS, 486, 4290
Baumgartner, W. H., Tueller, J., Markwardt, C. B., et al. 2013, ApJS, 207, 19
Bellocchi, E., Arribas, S., Colina, L., et al. 2013, A&A, 557, A59
Bellocchi, E., Villar Martín, M., Cabrera-Lavers, A., et al. 2019, A&A, 626, A89
Benson, A. J., Bower, R. G., Frenk, C. S., et al. 2003, ApJ, 599, 38
Bertin, E., & Arnouts, S. 1996, A&AS, 117, 393
Bessiere, P. S., Ramos Almeida, C., Holden, L. R., et al. 2024, A&A, 689, A271
Burtscher, L., Davies, R. I., Shimizu, T. T., et al. 2021, A&A, 654, A132
Bushouse, H., Eisenhamer, J., Dencheva, N., et al. 2023, spacetelescope/jwst: JWST v1.11.4, Zenodo, doi:10.5281/zenodo.8247246
Caglar, T., Burtscher, L., Brandl, B., et al. 2020, A&A, 634, A114
Cano-Díaz, M., Maiolino, R., Marconi, A., et al. 2012, A&A, 537, L8
Carniani, S., Marconi, A., Maiolino, R., et al. 2015, A&A, 580, A102
Cazzoli, S., Gil de Paz, A., Márquez, I., et al. 2020, MNRAS, 493, 3656
Cazzoli, S., Hermosa Muñoz, L., Márquez, I., et al. 2022, A&A, 664, A135
Chatzikos, M., Bianchi, S., Camilloni, F., et al. 2023, RMxAA, 59, 327
Cheung, E., Bundy, K., Cappellari, M., et al. 2016, Natur, 533, 504
Chisholm, J., Tremonti, C. A., Leitherer, C., et al. 2017, MNRAS, 469, 4831
Cicone, C., Maiolino, R., Sturm, E., et al. 2014, A&A, 562, A21
Concas, A., Popesso, P., Brusa, M., et al. 2019, A&A, 622, A188
D'Agostino, J. J., Kewley, L. J., Groves, B. A., et al. 2019, MNRAS, 487, 4153
Dale, D. A., Smith, J. D. T., Armus, L., et al. 2006, ApJ, 646, 161
Davé, R., Anglés-Alcázar, D., Narayanan, D., et al. 2019, MNRAS, 486, 2827
Davies, J. J., Crain, R. A., Oppenheimer, B. D., et al. 2020a, MNRAS, 491, 4462
Davies, R., Baron, D., Shimizu, T., et al. 2020b, MNRAS, 498, 4150
Davies, R. I., Burtscher, L., Rosario, D., et al. 2015, ApJ, 806, 127
Davies, R. I., Shimizu, T., Pereira-Santaella, M., et al. 2024, A&A, 689, A263
Di Matteo, T., Springel, V., & Hernquist, L. 2005, Natur, 433, 604
Draine, B. T. 2011, Physics of the Interstellar and Intergalactic Medium (Princeton, NJ: Princeton Univ. Press), 2011
Durré, M., & Mould, J. 2018, ApJ, 867, 149
Esparza-Arredondo, D., Ramos Almeida, C., Audibert, A., et al. 2024, A&A, submitted
Esposito, F., Alonso-Herrero, A., García-Burillo, S., et al. 2024, A&A, 686, A46
Fabian, A. C. 2012, ARA&A, 50, 455
Feltre, A., Gruppioni, C., Marchetti, L., et al. 2023, A&A, 675, A74
Ferland, G. J., Chatzikos, M., Guzmán, F., et al. 2017, RMxAA, 53, 385
Fernández-Ontiveros, J. A., Pérez-Montero, E., Vílchez, J. M., et al. 2021, A&A, 652, A23
Fiore, F., Feruglio, C., Shankar, F., et al. 2017, A&A, 601, A143
Fischer, T. C., Crenshaw, D. M., Kraemer, S. B., et al. 2011, ApJ, 727, 71
Fischer, T. C., Crenshaw, D. M., Kraemer, S. B., et al. 2013, ApJS, 209, 1
Fischer, T. C., Kraemer, S. B., Schmitt, H. R., et al. 2018, ApJ, 856, 102
Fischer, T. C., Machuca, C., Diniz, M. R., et al. 2017, ApJ, 834, 30
Fluetsch, A., Maiolino, R., Carniani, S., et al. 2019, MNRAS, 483, 4586
Förster Schreiber, N. M., Übler, H., Davies, R. L., et al. 2019, ApJ, 875, 21
Freeman, W. R., Siana, B., Kriek, M., et al. 2019, ApJ, 873, 102
García-Bernete, I., Alonso-Herrero, A., García-Burillo, S., et al. 2021, A&A, 645, A21
García-Bernete, I., Alonso-Herrero, A., Rigopoulou, D., et al. 2024a, A&A, 681, L7
García-Bernete, I., Pereira-Santaella, M., González-Alfonso, E., et al. 2024b, A&A, 682, L5
García-Bernete, I., Ramos Almeida, C., Acosta-Pulido, J. A., et al. 2016, MNRAS, 463, 3531
García-Bernete, I., Rigopoulou, D., Alonso-Herrero, A., et al. 2022a, A&A, 666, L5
García-Bernete, I., Rigopoulou, D., Alonso-Herrero, A., et al. 2022b, MNRAS, 509, 4256
García-Bernete, I., Rigopoulou, D., Donnan, F. R., et al. 2024c, A&A, in press (arXiv:2409.05686)
García-Burillo, S., Alonso-Herrero, A., Ramos Almeida, C., et al. 2021, A&A, 652, A98
García-Burillo, S., Combes, F., Ramos Almeida, C., et al. 2019, A&A, 632, A61
García-Burillo, S., Combes, F., Usero, A., et al. 2014, A&A, 567, A125
Gardner, J. P., Mather, J. C., Abbott, R., et al. 2023, PASP, 135, 068001
Gasman, D., Argyriou, I., Sloan, G. C., et al. 2023, A&A, 673, A102
Genzel, R., Lutz, D., Sturm, E., et al. 1998, ApJ, 498, 579
Hao, L., Strauss, M. A., Tremonti, C. A., et al. 2005, AJ, 129, 1783
Harrison, C. M. 2017, NatAs, 1, 0165
Harrison, C. M., Alexander, D. M., Mullaney, J. R., et al. 2014, MNRAS, 441, 3306
Harrison, C. M., Alexander, D. M., Mullaney, J. R., et al. 2016, MNRAS, 456, 1195
Harrison, C. M., Costa, T., Tadhunter, C. N., et al. 2018, NatAs, 2, 198
Harrison, C. M., & Ramos Almeida, C. 2024, Galax, 12, 17
Heckman, T. M., Armus, L., & Miley, G. K. 1990, ApJS, 74, 833
Hermosa Muñoz, L., Alonso-Herrero, A., & Pereira-Santaella, M. 2024a, A&A, in press (arXiv:2407.15807)
Hermosa Muñoz, L., Cazzoli, S., Márquez, I., et al. 2024b, A&A, 683, A43
Hervella Seoane, K., Ramos Almeida, C., Acosta-Pulido, J. A., et al. 2023, A&A, 680, A71
Hopkins, P. F., Hernquist, L., Cox, T. J., et al. 2008, ApJS, 175, 356
Houck, J. R., Roellig, T. L., van Cleve, J., et al. 2004, ApJS, 154, 18
Kakkad, D., Mainieri, V., Vietri, G., et al. 2020, A&A, 642, A147
Kakkad, D., Sani, E., Rojas, A. F., et al. 2022, MNRAS, 511, 2105
King, A., & Pounds, K. 2015, ARA&A, 53, 115
Krajnović, D., Cappellari, M., de Zeeuw, P. T., et al. 2006, MNRAS, 366, 787
Labiano, A., Argyriou, I., Álvarez-Márquez, J., et al. 2021, A&A, 656, A57
Labiano, A., Azzollini, R., Bailey, J., et al. 2016, Proc. SPIE, 9910, 99102W
Lamperti, I., Pereira-Santaella, M., Perna, M., et al. 2022, A&A, 668, A45
Law, D. R. E., Morrison, J., Argyriou, I., et al. 2023, AJ, 166, 45
Leung, G. C. K., Coil, A. L., Aird, J., et al. 2019, ApJ, 886, 11
Liu, G., Zakamska, N. L., Greene, J. E., et al. 2013, MNRAS, 436, 2576
Luridiana, V., Morisset, C., & Shaw, R. A. 2015, A&A, 573, A42
Maksym, W. P., Elvis, M., Fabbiano, G., et al. 2023, ApJ, 951, 146
McCarthy, I. G., Schaye, J., Bower, R. G., et al. 2011, MNRAS, 412, 1965
McElroy, R., Croom, S. M., Pracy, M., et al. 2015, MNRAS, 446, 2186
McNamara, B. R., & Nulsen, P. E. J. 2007, ARA&A, 45, 117
Meenakshi, M., Mukherjee, D., Wagner, A. Y., et al. 2022, MNRAS, 516, 766
Melioli, C., Brighenti, F., & D'Ercole, A. 2015, MNRAS, 446, 299
Morganti, R., Tsvetanov, Z. I., Gallimore, J., et al. 1999, A&AS, 137, 457

Morisset, C., Delgado-Inglada, G., & Flores-Fajardo, N. 2015, RMxAA, 51, 103
Mukherjee, D., Bicknell, G. V., Wagner, A. Y., et al. 2018a, MNRAS, 479, 5544
Mukherjee, D., Wagner, A. Y., Bicknell, G. V., et al. 2018b, MNRAS, 476, 80
Müller-Sánchez, F., Prieto, M. A., Hicks, E. K. S., et al. 2011, ApJ, 739, 69
Nagar, N. M., Wilson, A. S., Mulchaey, J. S., et al. 1999, ApJS, 120, 209
Nyland, K., Harwood, J. J., Mukherjee, D., et al. 2018, ApJ, 859, 23
Orienti, M., & Prieto, M. A. 2010, MNRAS, 401, 2599
Page, M. J., Symeonidis, M., Vieira, J. D., et al. 2012, Natur, 485, 213
Peralta de Arriba, L., Alonso-Herrero, A., García-Burillo, S., et al. 2023, A&A, 675, A58
Pereira-Santaella, M., Álvarez-Márquez, J., García-Bernete, I., et al. 2022, A&A, 665, L11
Pereira-Santaella, M., Diamond-Stanic, A. M., Alonso-Herrero, A., et al. 2010, ApJ, 725, 2270
Pereira-Santaella, M., García-Bernete, I., González-Alfonso, E., et al. 2024, A&A, 685, L13
Pereira-Santaella, M., Rigopoulou, D., Farrah, D., et al. 2017, MNRAS, 470, 1218
Pérez-Díaz, B., Pérez-Montero, E., Fernández-Ontiveros, J. A., et al. 2022, A&A, 666, A115
Ramos Almeida, C., Bischetti, M., García-Burillo, S., et al. 2022, A&A, 658, A155
Ramos Almeida, C., Esparza-Arredondo, D., González-Martín, O., et al. 2023, A&A, 669, L5
Ramos Almeida, C., Sánchez-Portal, M., Pérez García, A. M., et al. 2011, MNRAS, 417, L46
Ricci, C., Trakhtenbrot, B., Koss, M. J., et al. 2017, ApJS, 233, 17
Rieke, G. H., Wright, G. S., Böker, T., et al. 2015, PASP, 127, 584
Riffel, R. A., Storchi-Bergmann, T., Riffel, R., et al. 2023, MNRAS, 521, 1832
Rigby, J., Perrin, M., McElwain, M., et al. 2023, PASP, 135, 048001
Roberts-Borsani, G. W., Saintonge, A., Masters, K. L., et al. 2020, MNRAS, 493, 3081
Rubin, K. H. R., Prochaska, J. X., Koo, D. C., et al. 2014, ApJ, 794, 156
Rupke, D. S., Veilleux, S., & Sanders, D. B. 2005, ApJ, 632, 751
Rupke, D. S. N., & Veilleux, S. 2011, ApJL, 729, L27

Ruschel-Dutra, D., Storchi-Bergmann, T., Schnorr-Müller, A., et al. 2021, MNRAS, 507, 74
Sajina, A., Lacy, M., & Pope, A. 2022, Univ, 8, 356
Schawinski, K., Thomas, D., Sarzi, M., et al. 2007, MNRAS, 382, 1415
Shapley, A. E., Steidel, C. C., Pettini, M., et al. 2003, ApJ, 588, 65
Shimizu, T. T., Davies, R. I., Lutz, D., et al. 2019, MNRAS, 490, 5860
Smajić, S., Fischer, S., Zuther, J., et al. 2012, A&A, 544, A105
Somerville, R. S., & Davé, R. 2015, ARA&A, 53, 51
Speranza, G., Ramos Almeida, C., Acosta-Pulido, J. A., et al. 2024, A&A, 681, A63
Sun, A.-L., Greene, J. E., & Zakamska, N. L. 2017, ApJ, 835, 222
Sun, S., Guainazzi, M., Ni, Q., et al. 2018, MNRAS, 478, 1900
Sutherland, R. S., & Dopita, M. A. 2017, ApJS, 229, 34
Thean, A., Pedlar, A., Kukula, M. J., et al. 2000, MNRAS, 314, 573
Theureau, G., Hanski, M. O., Coudreau, N., et al. 2007, A&A, 465, 71
Thomas, A. D., Dopita, M. A., Shastri, P., et al. 2017, ApJS, 232, 11
U, V., Lai, T., Bianchin, M., et al. 2022, ApJL, 940, L5
Ulivi, L., Venturi, G., Cresci, G., et al. 2024, A&A, 685, A122
Veilleux, S., Cecil, G., & Bland-Hawthorn, J. 2005, ARA&A, 43, 769
Veilleux, S., Maiolino, R., Bolatto, A. D., et al. 2020, A&ARv, 28, 2
Veilleux, S., Meléndez, M., Sturm, E., et al. 2013, ApJ, 776, 27
Venturi, G., Cresci, G., Marconi, A., et al. 2021, A&A, 648, A17
Venturi, G., Treister, E., Finlez, C., et al. 2023, A&A, 678, A127
Weinberger, R., Springel, V., Hernquist, L., et al. 2017, MNRAS, 465, 3291
Weiner, B. J., Coil, A. L., Prochaska, J. X., et al. 2009, ApJ, 692, 187
Wells, M., Pel, J.-W., Glasse, A., et al. 2015, PASP, 127, 646
Werner, M. W., Roellig, T. L., Low, F. J., et al. 2004, ApJS, 154, 1
Winkel, N., Husemann, B., Singha, M., et al. 2023, A&A, 670, A3
Wright, G. S., Rieke, G. H., Glasse, A., et al. 2023, PASP, 135, 048003
Wright, G. S., Wright, D., Goodson, G. B., et al. 2015, PASP, 127, 595
Zhang, L., García-Bernete, I., Packham, C., et al. 2024, ApJL, in press
Zhang, L., & Ho, L. C. 2023, ApJL, 953, L9
Zhang, L., Ho, L. C., & Li, A. 2022, ApJ, 939, 22
Zhang, L., Ho, L. C., & Xie, Y. 2021, AJ, 161, 29
Zoghbi, A., Matt, G., Miller, J. M., et al. 2017, ApJ, 836, 2
Zubovas, K., & Nardini, E. 2020, MNRAS, 498, 3633